frontiers in Materials

TYPE Original Research
PUBLISHED 27 March 2026
DOI 10.3389/fmats.2026.1762995

OPEN ACCESS

EDITED BY
Giovanna Xotta,
University of Padua, Italy

REVIEWED BY
Rami Alsodi,
Department of Public Works, United Arab Emirates
Yasitha Alahakoon,
University of Peradeniya, Sri Lanka

*CORRESPONDENCE
Inkyu Rhee,
rheei@jnu.ac.kr

RECEIVED 08 December 2025
REVISED 09 February 2026
ACCEPTED 24 February 2026
PUBLISHED 27 March 2026

CITATION
Park H-J, Choe Y, Kim D-G and Rhee I (2026) Integrated formwork removal decision framework for concrete slabs using FBG sensors and machine learning.
Front. Mater. 13:1762995.
doi: 10.3389/fmats.2026.1762995

Integrated formwork removal decision framework for concrete slabs using FBG sensors and machine learning

Hyoung-Jun Park[1], Yubin Choe[1], Dae-Gil Kim[1] and Inkyu Rhee[2]*

[1]Honam Research Division, Electronics and Telecommunications Research Institute, Gwangju, Republic of Korea, [2]Department of Civil Engineering, Chonnam National University, Gwangju, Republic of Korea

Accurate prediction of early-age concrete strength is critical for ensuring construction safety and optimizing formwork removal schedules. This study presents an integrated decision-making framework for curing quality management, employing Fiber Bragg Grating (FBG) sensors to monitor internal temperature and drying shrinkage for 28 days. To validate hydration kinetics, a thermo-mechanical coupled analysis was conducted, and a machine learning framework using Gradient Boosting was explored to predict compressive strength. The results indicated that a literature-based dataset limited to 55 points led to an R^2 approaching 1, revealing inherent overfitting due to reliance on ambient rather than internal core temperatures. These observed deviations highlight the necessity of in-situ monitoring. The study concludes that enhancing predictive robustness requires larger datasets synchronized with internal hydration heat records to mitigate overfitting in field applications.

KEYWORDS
concrete maturity, concrete slab, coupled thermo-mechanical analysis, form removal, machine learning, fiber bragg grating sensor

1 Introduction

Predicting the compressive strength of concrete structures remains a complex engineering challenge due to the combined effects of environmental factors, binder composition, and structural geometry. Laboratory-cast specimens, typically cured under standardized conditions, provide controlled reference data but often fail to reflect the actual in-situ performance of structural elements. In practice, curing conditions are highly non-uniform, with spatial and temporal temperature variations resulting from the exothermic heat of cement hydration. These thermal gradients, further influenced by member size, shape, boundary conditions, and exposure environment, directly affect hydration kinetics and microstructural development. Consequently, the strength gain of field structures often diverges from laboratory predictions, even when identical mix proportions are employed. This discrepancy highlights the limitations of conventional specimen-based testing and underscores the need for advanced predictive approaches that explicitly account for thermal history (time–temperature profile during curing), maturity effects, and field-specific boundary conditions (Han and Zhang, 2016). The maturity method represents one of the most effective approaches to address these challenges, as it integrates the thermal history of concrete into strength prediction. Early formulations,

such as the Nurse–Saul model, assumed a linear relationship between maturity and strength, offering computational simplicity but leading to significant inaccuracies under low-temperature curing (McIntosh, 1956; Chengju, 1989; De Schutter et al., 1996; Carino and Tank, 1990; Yang et al., 2016; Jin et al., 2017; Wang et al., 2019). The Arrhenius model improved predictive accuracy by accounting for nonlinear temperature effects on hydration kinetics, though its mathematical complexity initially limited widespread field application (Carino and Tank, 1990; Carino and Lew, 2001; Tank and Carino, 1991; Chen, 2007). More recently, logarithmic and other nonlinear regression models have been introduced to better capture the maturity–strength relationship while requiring relatively limited calibration data, thereby extending their applicability across diverse curing environments (Rusna and Kalpana, 2022; Bakhoum et al., 2023; Dewan et al., 2023). Recent research has strengthened the role of maturity-based prediction through integration with digital technologies and sustainability-driven practices. Kazemifard et al. (2024) applied the maturity method to self-compacting concrete, achieving over 94% prediction accuracy without secondary calibration. Cheng et al. (2021) demonstrated its sensitivity to mixture parameters, showing that strength increased with decreasing water-to-binder ratios. Kampli et al. (2023), Miller et al. (2023), and Kim et al. (2024) integrated the maturity method with IoT-enabled monitoring systems, achieving strong correlations between predicted and measured strengths and ensuring stable early-age predictions under field conditions. From a sustainability perspective, Imran et al. (2022) combined the maturity method with multivariate regression for eco-friendly concrete mixtures, outperforming conventional empirical approaches. These advancements underscore the maturity method's evolving role as both a predictive tool for mix design and a platform for real-time, sensor-driven construction management. Accurate prediction of early-age concrete strength is critical for ensuring construction safety and optimizing formwork removal schedules. This study presents an integrated decision-making framework for the curing quality management of horizontal concrete members, specifically slabs. Fiber Bragg Grating (FBG) sensors were embedded to monitor the internal temperature history and drying shrinkage strain of concrete specimens for 28 days. A one-way unreinforced concrete slab measuring 1 m in width, 3 m in length, and 0.2 m in thickness was cast. The generation and gradual dissipation of internal hydration temperature in hot/normal weather concrete according to external environmental conditions were monitored using sensors, and the maturity was quantitatively evaluated. Additionally, drying shrinkage strain that may occur during the early hardening process of concrete was examined. Distributed FBG sensors were employed for temperature and strain measurements. For age-specific strength determination, both separately cured specimens and core samples extracted from the slab were tested to measure the strength at various ages. To validate the hydration kinetics, a thermo-mechanical coupled analysis with relative humidity records was conducted, correlating heat transfer trends with mechanical strain behavior. Finally, a machine learning (ML)-based framework was developed to predict compressive strength by integrating experimental data with established maturity functions.

2 Test setup and sensor measurement

2.1 Test setup

The primary objective of this study is to monitor and manage the curing quality of horizontal structural concrete members, specifically concrete slabs, during the construction phase. To facilitate engineering decision-making regarding the optimal timing for formwork removal based on curing quality, it is imperative to measure the core temperature within the concrete member. In cases involving large-scale or complex members, measuring core temperatures at spatially distributed internal points becomes essential. This approach is particularly applicable to the construction of large-scale residential complexes, contributing to stable construction management. Concrete maturity can be computed using the in-situ core temperature history recorded during curing. Utilizing established methods such as the Nurse-Saul linear function or the Arrhenius-based non-linear function allows for the estimation of strength development and, consequently, the determination of the appropriate timing for formwork removal. The concept of concrete maturity quantifies the combined effects of time and temperature on strength development. It provides a non-destructive methodology for predicting the in-situ strength of concrete. The fundamental premise is that elevated temperatures accelerate hydration kinetics, resulting in a more rapid increase in strength. The maturity-based approach is well-established in international practice. In the United States, the maturity method is standardized in ASTM C1074 (2020) and incorporated into ACI 318-19 (2025), ACI PRC-347-14 (2021), and ACI 228.1R-19 (2019); formwork removal is generally permitted when concrete reaches approximately 70% of the specified design compressive strength, f'_c, corresponding to a maturity value of 300 °C–400 °C·h. In Europe, EN 13670 (2009) and EN 206 (2013) allow for early removal based on verified in-situ strength (typically 2–5 MPa or 50%–70% of f'_c), with maturity values ranging from 200 °C to 500 °C·h. Japanese standards (JSCE-GC No. 16, 2007) typically require a minimum strength of 5 MPa and a maturity exceeding 300 °C·h. In South Korea, the KCI Concrete Standard (KCS 14 20 12) impose stricter criteria, mandating formwork removal only after the concrete reaches a compressive strength for slab construction (horizontal formwork). 5 MPa minimum, and 14 MPa minimum or 2/3 of design strength, whichever greater is considered a practical threshold for form removal, while supports (shores) are removed only after reaching 100% of f'_c. Table 1 summarized these standards associated with concrete maturity.

Accurate, long-term monitoring of the internal core temperature is critical for predicting curing quality during construction. This study employs distributed fiber optic sensors embedded within concrete slabs with relatively large surface areas. When utilizing bare FBG sensors without adequate protective mechanisms, the sensors are susceptible to initial damage during concrete placement. Furthermore, long-term exposure renders them vulnerable to durability degradation or failure due to mechanical friction with concrete aggregates or chemical deterioration. Additionally, exposed FBGs are simultaneously influenced by the heat of hydration and strains resulting from the shrinkage and expansion of the concrete during curing. These coupled factors cause fluctuations in the Bragg wavelength, thereby compromising the accuracy of hydration

TABLE 1 Comparison of standards and practices: Concrete maturity vs. Formwork removal.

Standard/Code	Formwork removal (threshold)	Shore removal	Typical maturity index	Research trends
ASTM C1074 ACI 318 ACI 347R	≈70% f_c' for slabs and beams	100% f_c'	~300 °C–400 °C·h	Focus on field calibration, embedded sensors, reliability under variable curing
EN 13670 EN 1992-1-1 EN 206	2–5 MPa or 50%–70% f_c' (in-situ strength)	~100% f_c'	~200 °C–500 °C·h	Strong interest in sustainability, improved maturity models, accelerated construction cycles
JSCE-GC No. 16 JSCE standards	≥5 MPa and maturity ≥300 °C·h	100% f_c'	~300 °C·h	Hybrid approaches (maturity + ultrasonic/rebound hammer), BIM integration
KCI-KCS 14 20 12	≥ Max (14 MPa, 2/3 f′c)	100% f_c'	~300 °C·h (limit: 5 MPa)	Strong push for IoT, smart sensors, and AI-driven decision support

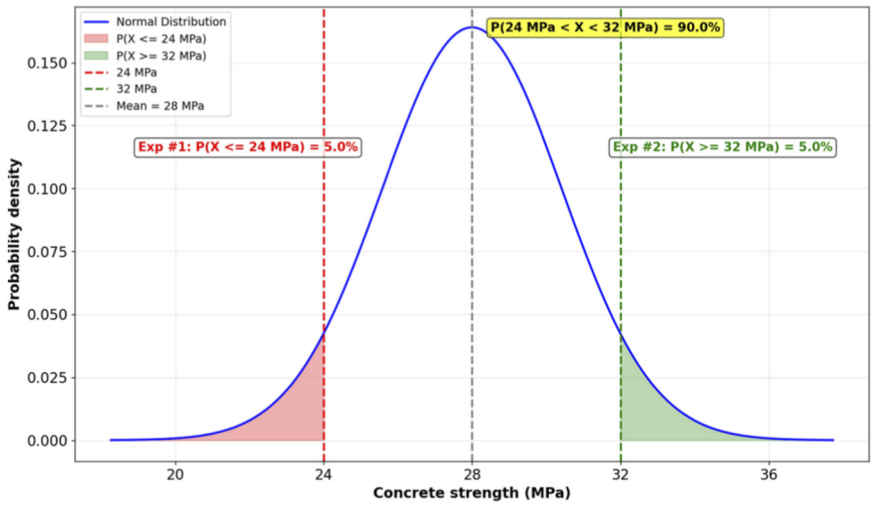

FIGURE 1
Exp #1 and #2: corresponds to the lower 5-th and upper 5-th percentiles of the 28-day strength distribution.

TABLE 2 Mix design for unreinforced concrete slab specimens (per m^3).

Test No.	Cement (kg)	Gravel (kg)	Sand (kg)	Water (kg)	W/C	Water reducer (%)	Target strength (MPa)
Exp #1	305	960	800	196	0.64	-	24
Exp #2	400	1,040	680	175	0.44	0.328%	32

heat measurements derived from FBG sensors. To address these challenges, this study utilized FBG sensors packaged in stainless steel (SUS) tubes. The SUS tube acts as a buffer against mechanical deformation and effectively isolates the sensor from concrete-induced strains, enabling the measurement of pure hydration heat. Furthermore, by preventing direct contact with aggregates, the packaging enhances the durability and reliability of the sensors during long-term monitoring. To validate the performance of the SUS-packaged FBG sensors and to monitor core temperature and drying shrinkage strain during curing, concrete slab specimens were fabricated with dimensions of 3 m × 1 m × 0.2 m. The concrete utilized was of grade C20/25 (24 MPa), with two distinct mix designs applied across two experimental batches. As detailed in Figure 1; Table 2, the mix designs were formulated to correspond to the lower 5-th and upper 5-th percentiles of the 28-day strength distribution. Consequently, the target compressive strength was set at 24 MPa for the first experiment and 32 MPa for the second, with a mean target compressive strength of 28 MPa.

Multiple FBG sensors were embedded at the mid-depth (0.1 m) of the slab. Additionally, two strain sensors were installed to monitor the drying shrinkage strain history during hydration in both the longitudinal and transverse directions, as indicated in Figures 2, 3.

10.3389/fmats.2026.1762995

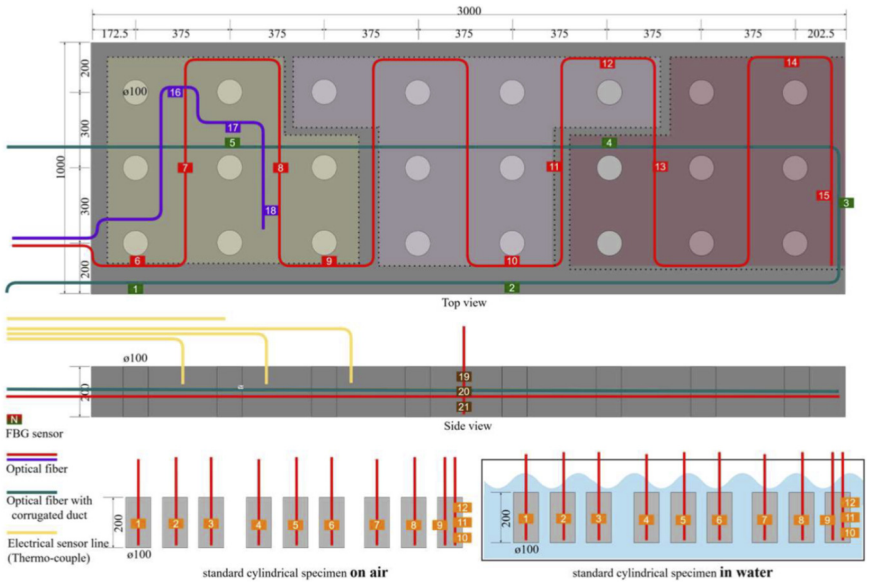

FIGURE 2
Test specimen layout and FBG sensors arrangement to measuring the temperature and shrinkage strain.

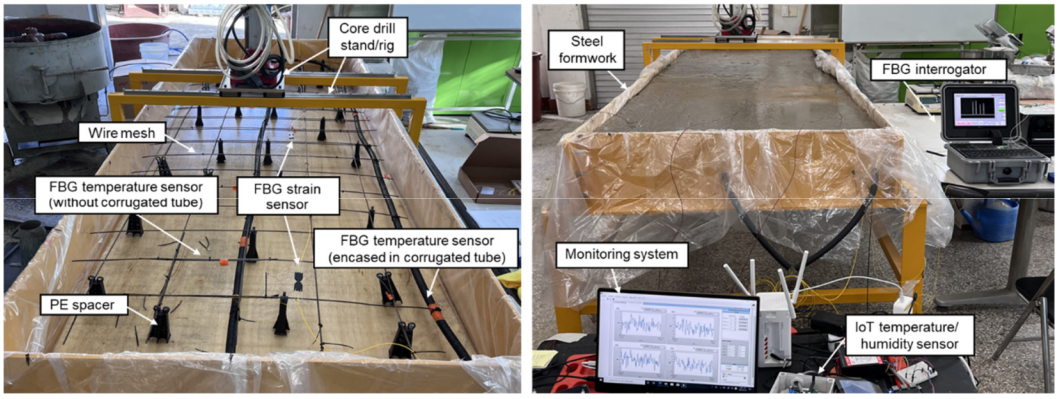

FIGURE 3
Concrete slab specimen: **(a)** arranged FBG sensors for measuring temperature and drying shrinkage strain in the formwork, **(b)** interrogating the data from the embedded sensors after the casting.

Ten sensors were installed to record the thermal history of the slab's core and surface. Control specimens (Ø 100 × 200 mm cylinders) were cast simultaneously and cured under standard and air-dry conditions. Strength development was verified at 3, 7, 14 and 28 days using extracted cores, standard-cured cylinders, and air-cured cylinders.

Additionally, surface temperatures were verified using infrared thermography. For Experiments #1 and #2, the initial temperatures of the fresh concrete were 25 °C and 17.5 °C, respectively. The laboratory ambient temperatures were maintained at averages of 28 °C and 16.5 °C, respectively, throughout the 28-day period. To evaluate compressive strength at ages of 3, 7, 14 and 28 days, core samples (Ø 100 × 200 mm cylinders) were extracted from the slab. Furthermore, cylindrical control specimens were prepared for both air-drying and water-curing conditions (three specimens per condition). Internal temperature data for these specimens was logged at 2-min intervals to monitor the curing environment. Finally, indirect strength estimation was performed at 28 days using a Schmidt hammer (rebound hammer) as a non-destructive testing method.

2.2 FBG sensor measurement

The temperature and strain sensors operated with central wavelengths ranging from 1,542.7 nm to 1,566.3 nm. Ambient temperature and humidity data were logged at 2-min intervals. A FBG consists of a periodic modulation of the refractive index

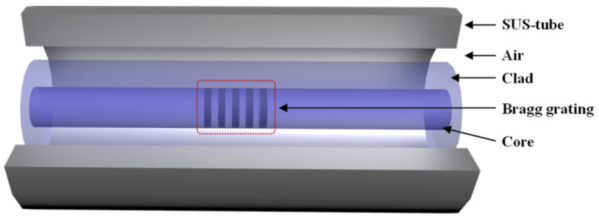

FIGURE 4
SUS-tube-packaged FBG.

within the fiber core (He et al., 2021). This structure reflects a specific wavelength of the incident light while transmitting the remaining wavelengths (Kim et al., 2021). The reflected wavelength, known as the Bragg wavelength, is defined in Equation 1 (Di Palma et al., 2022):

$$\lambda_{\text{Bragg}} = 2 \times n_{\text{eff}} \times \Lambda_{\text{g}} \tag{1}$$

where Λ_{g} denotes the grating period and n_{eff} represents the effective refractive index of the fiber core. The Bragg wavelength of an FBG varies in response to external stimuli, with temperature changes and strain being the most significant influencing factors. The corresponding shift in the Bragg wavelength ($\Delta\lambda_{\text{Bragg}}$) can be expressed in Equations 2–4 (Qiao et al., 2023):

$$\Delta\lambda_{\text{Bragg}} = \mu_s \Delta\varepsilon + \mu_T \Delta T \tag{2}$$

$$\mu_s = (1 - \rho_e)\lambda_B \tag{3}$$

$$\mu_T = (\alpha_F + \xi)\lambda_B \tag{4}$$

where μ_s, $\Delta\varepsilon$, μ_T, ΔT, α_F, ξ, and ρ_e denote the strain sensitivity of the Bragg wavelength shift, strain variation, temperature sensitivity of the Bragg wavelength shift, temperature change, thermal expansion coefficient of the optical fiber, thermo-optic coefficient of the optical fiber, and elasto-optic coefficient of the optical fiber, respectively. The variation in the reflected Bragg wavelength can be directly measured (Li et al., 2021), or the light intensity can be monitored using an optical edge filter (Ji et al., 2022), enabling the application of FBGs as temperature and strain sensors. When a bare FBG is utilized without adequate protection, its durability may be compromised, rendering it susceptible to damage from friction with concrete aggregates. Furthermore, a bare FBG is simultaneously influenced not only by the heat of hydration generated during curing but also by the strain induced by the shrinkage and expansion of the concrete. These coupled factors induce complex shifts in the Bragg wavelength, thereby reducing the accuracy of hydration heat measurements. To address this issue, the FBG sensors in this study were packaged within a stainless-steel (SUS) tube as illustrated in Figure 4.

The SUS tube acts as a buffer against mechanical deformation and effectively decouples the sensor from concrete-induced strain, enabling the measurement of temperature changes solely attributable to hydration heat. Additionally, the packaging prevents direct contact with aggregates, enhancing the sensor's durability and reliability for long-term monitoring. To assess the efficacy of the packaging, a comparative experiment was conducted to evaluate the temperature sensitivity of the SUS-packaged FBG against that of a bare FBG. Figure 5 presents both the experimental setup and the obtained results. In the experimental setup, a bare FBG and three SUS-tube-packaged FBGs were placed on a temperature-controlled plate (HnC-20–110), and their Bragg wavelength shifts were simultaneously recorded using a commercial FBG interrogator (I-MON 512). The experiment was conducted by decreasing the temperature from 110 °C to −10 °C in 20 °C decrements. At each temperature step, the sensors were stabilized for 10 min to ensure thermal equilibrium before the Bragg wavelength was recorded. The results demonstrated that the Bragg wavelengths of all four sensors exhibited a linear relationship with temperature. The temperature sensitivity of the bare FBG was measured to be 10.84 pm/°C, which is consistent with the well-known value of approximately 11 pm/°C for a bare FBG (Hill and Meltz, 2002). In contrast, the SUS-tube-packaged FBGs exhibited slightly lower sensitivities of 9.06 pm/°C, 9.45 pm/°C, and 8.93 pm/°C for SUS FBG 1, SUS FBG 2, and SUS FBG 3, respectively. On average, the sensitivity of the packaged sensors was approximately 15.6% lower than that of the bare FBG. This reduction is attributed to the thermal buffering effect of the SUS tube, which limits direct heat transfer to the fiber compared to the directly exposed bare FBG. Although the sensitivity of the SUS-tube-packaged FBGs is lower, it remains sufficient for the accurate measurement of hydration heat.

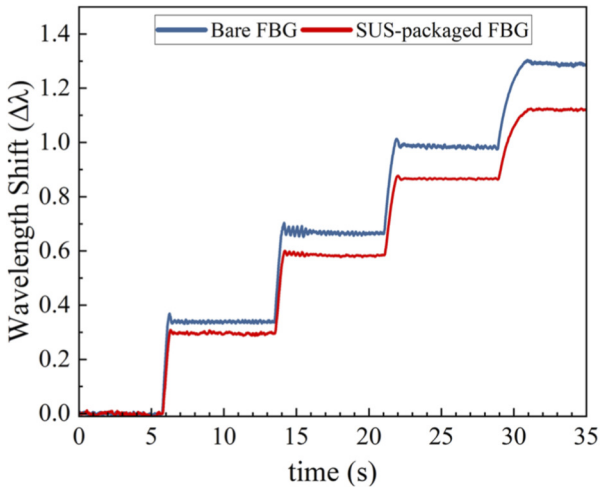

FIGURE 5
Sensitivity of the SUS-tube-packaged FBGs vs. Bare FBG sensors.

3 Test results

3.1 Hydration process based on temperature monitoring

The surface temperature data obtained from infrared thermography reveals that the concrete temperature begins at 25 °C, and 17.5 °C for Exp #1, and 2 and rises rapidly during the initial curing period as shown in Figure 6. The peak temperature of

10.3389/fmats.2026.1762995

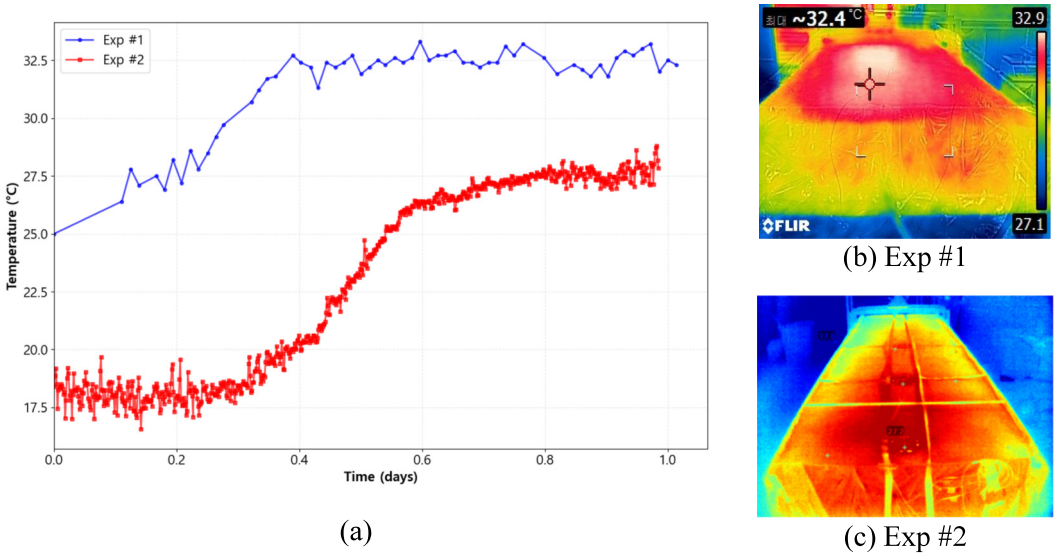

FIGURE 6
Surface temperature by infrared camera (Exp #1, #2): **(a)** Surface temperature for day 1 after casting, **(b)** 32.4 °C at 1 day (24 h), **(c)** 27.2 °C at 1 day (24 h).

36.4 °C, reached at 14.4 h for Exp #1, 31.8 °C, reached at 0.8 h for Exp #2 corresponds to the most intensive phase of cement hydration, primarily driven by the reaction of tricalcium silicate (C3S) and, to a lesser extent, dicalcium silicate (C2S).

The observed temperature rise of 11.4 °C, 14.3 °C for Exp #1 and #2 is characteristic of hydration heat generation under summer/fall slab conditions, indicating vigorous chemical activity within the concrete matrix while the relative humidity was 51%–52% in average. Internal temperature measurements from the FBG sensors demonstrate consistently higher values compared to surface temperatures measured by infrared thermography as shown in Figure 7.

This gradient reflects the internal heat generation and its subsequent dissipation to the external environment. While all sensors exhibited similar temperature evolution patterns, subtle variations among monitoring locations highlight the influence of slab thickness, sensor positioning, and boundary conditions on local thermal development. The temperature gradient analysis provides quantitative insight into hydration kinetics. The maximum temperature differential of 2.53 °C, 4.37 °C for Exp #1, and #2 serves as a direct indicator of reaction intensity. The peak differential at 0.667 days (16 h), 0.938 days (22.5 h) for Exp #1, and #2 corresponds to the primary reaction phase of C3S, while the subsequent gradual decrease indicates the deceleration of reaction rates as available cement compounds are consumed. The sustained temperature differential of 0 °C–4.37 °C maintained during the 2–4 day period reflects ongoing C2S hydration and secondary reactions of tricalcium aluminate (C3A). This phase represents the most active period for strength development, during which the majority of mechanical properties evolve. The chemical processes at this stage govern the formation of calcium silicate hydrate (C-

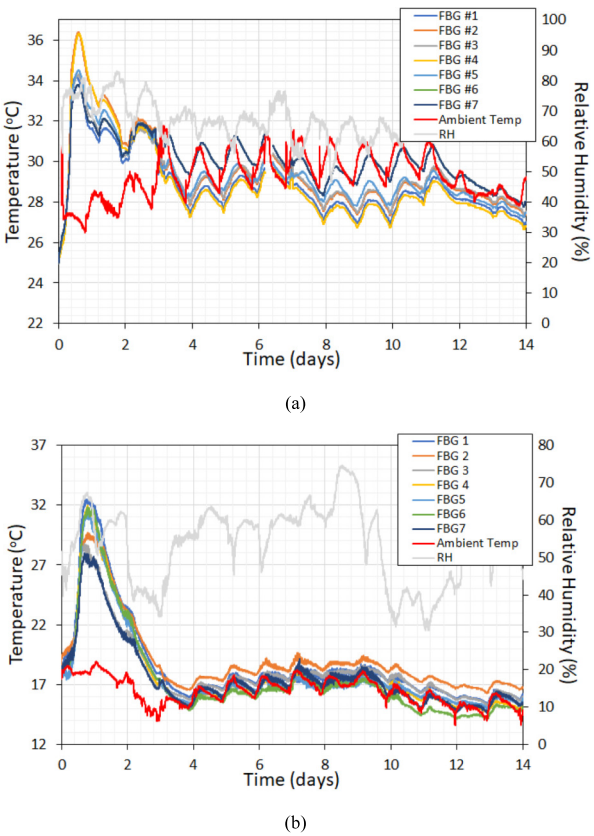

FIGURE 7
Temperature and RH data measured by FBG sensors: **(a)** Exp #1, **(b)** Exp #2.

S-H) gel, the primary binding agent in hardened concrete. The significant reduction in the temperature differential 0 °C after average Day 3 marks the transition from primary hydration to long-term hydration processes. This thermal behavior suggests that the major exothermic reactions have largely concluded and internal heat generation has substantially diminished. Consequently, the alignment of concrete temperature with ambient temperature variations demonstrates that environmental thermal effects have begun to dominate over internal heat generation. The periodic fluctuations observed during Days 4–5 reflect diurnal temperature cycles, indicating that the concrete has entered a phase where it responds sensitively to environmental changes rather than internal chemical reactions. Based on the observed thermal evolution, the degree of hydration at the peak temperature (16, 22 h) is estimated at approximately 30%–40%, while the 3-day mark represents 70%–80% completion. These estimates align well with established maturity-strength relationships, validating the hydration kinetics observed. The timing of the maximum temperature differential corresponds to the critical transition from a plastic to a hardened state, marking the onset of rapid strength gain. The subsequent thermal stabilization after Day 3 indicates the completion of the primary hydration reactions necessary for structural strength. Thus, this thermal signature provides critical data for construction scheduling, quality control, and decision-making regarding formwork removal.

3.2 Compressive strength gain and maturity

This study presents a comprehensive analysis of concrete compressive strength development under different curing conditions. The testing program included core samples extracted from field concrete and laboratory-prepared specimens subjected to air-dried (AD) and standard cured (SC) conditions. All specimens were cylindrical with dimensions of 100 mm diameter × 200 mm height, tested at 3, 7, and 28 days for Exp #1 and 1, 3, 7, 14 and 28 days for Exp #2. Figure 8 illustrates the temporal evolution of compressive strength for standard cured (SC), air-dried (AD), and in-situ cored specimens across curing ages of 1, 3, 7, 14, and 28 days.

The experimental results for both the 24 MPa (Exp #1) and 32 MPa (Exp #2) target mixtures demonstrate that SC specimens generally exhibit superior strength development compared to the AD and cored counterparts. Specifically, while the in-situ cored samples showed a strength reduction relative to the standard curing condition, they consistently satisfied the critical formwork removal threshold of 14 MPa by Day 3, verifying early-age structural stability. Figure 9 shows that the cored samples out of the slab specimen while curing at the age of 3, 7, 14, and 28 days. Figure 10 presents a stochastic analysis of strength variability using Probability Density Functions (PDFs) derived from the experimental data. The statistical comparison indicates that the SC regime yields the highest mean compressive strength ($\mu \approx 30.18$ MPa), whereas the AD and cored samples exhibit lower mean values of approximately 27.69 MPa and 26.96 MPa, respectively. The probability distributions quantify the reliability of the concrete performance; notably, the SC samples demonstrate a higher probability of exceeding the target design strength, P(X) ≥ 32 MPa compared to the cored samples, which display a distribution shifted towards the lower strength range. This discrepancy highlights the impact of field curing conditions on the probabilistic reliability of in-situ concrete strength compared to standardized laboratory specimens.

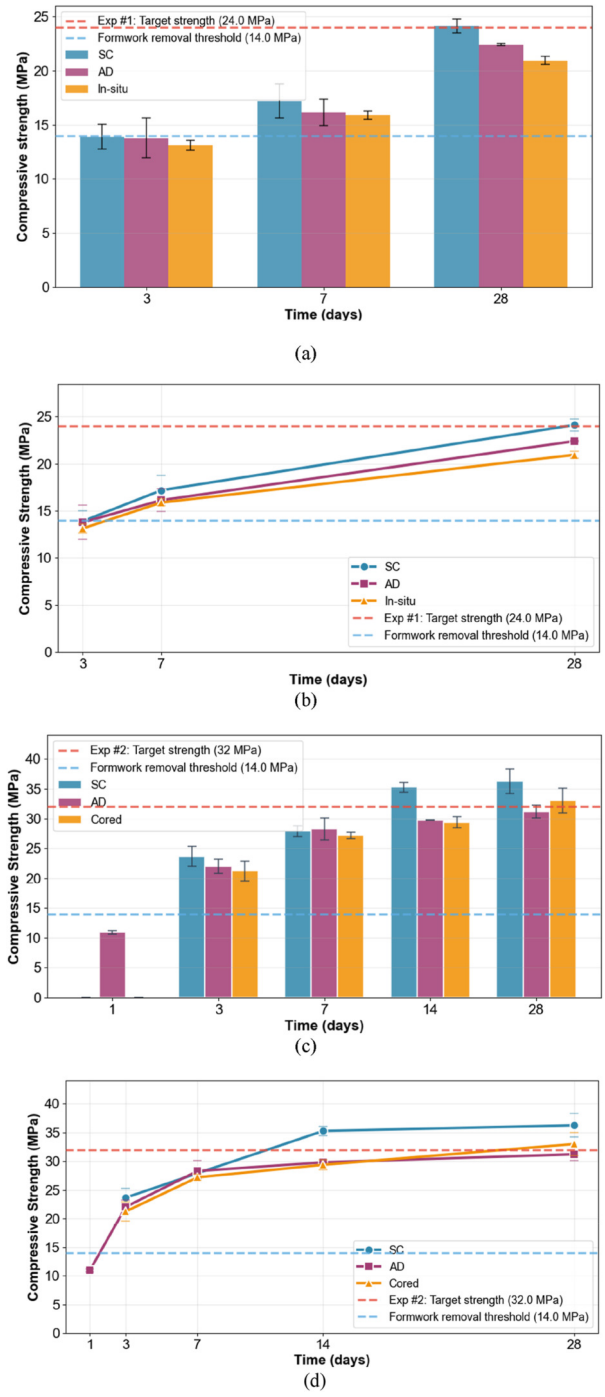

FIGURE 8
Compressive strength for Day 1, 3, 7, 14 and 28, Exp #1: **(a)** Compressive strength, **(b)** Target strength gaining % for 24 MPa, Exp #2: **(c)** Compressive strength, **(d)** Target strength gaining % for 32 MPa.

The non-destructive compressive strength testing of the concrete slab was conducted using the Proceq CH/Schmidt Hammer F-650. The test involved taking 56 rebound readings from the underside of

10.3389/fmats.2026.1762995

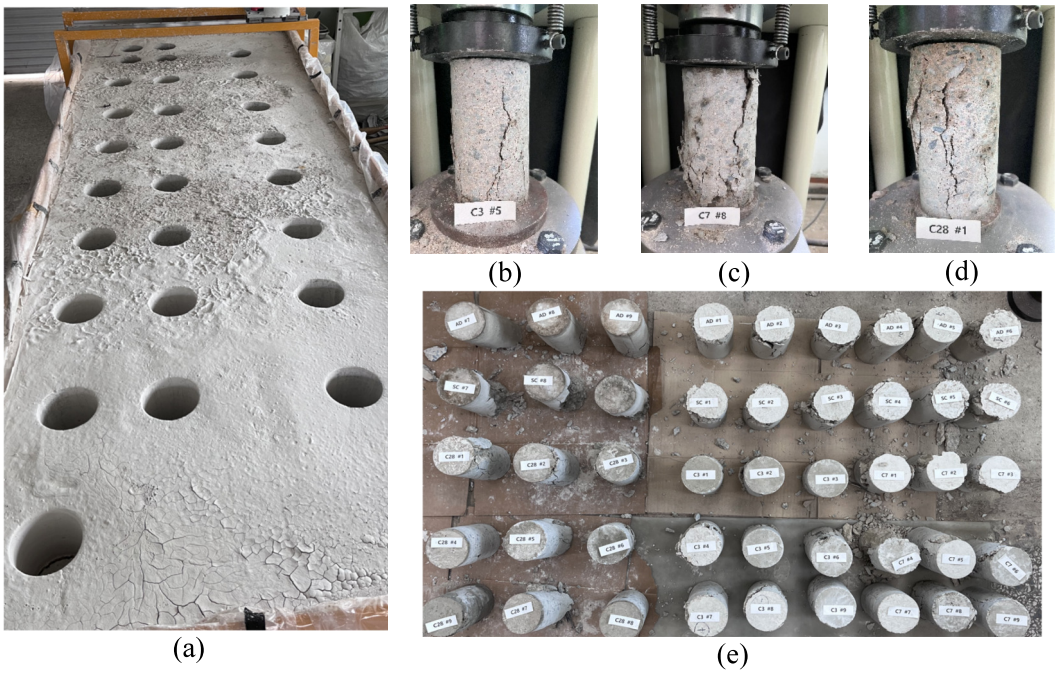

FIGURE 9
Compressive strength test: **(a)** cored slab, **(b–d)** uniaxial test, **(e)** SC, AD, and Cored samples.

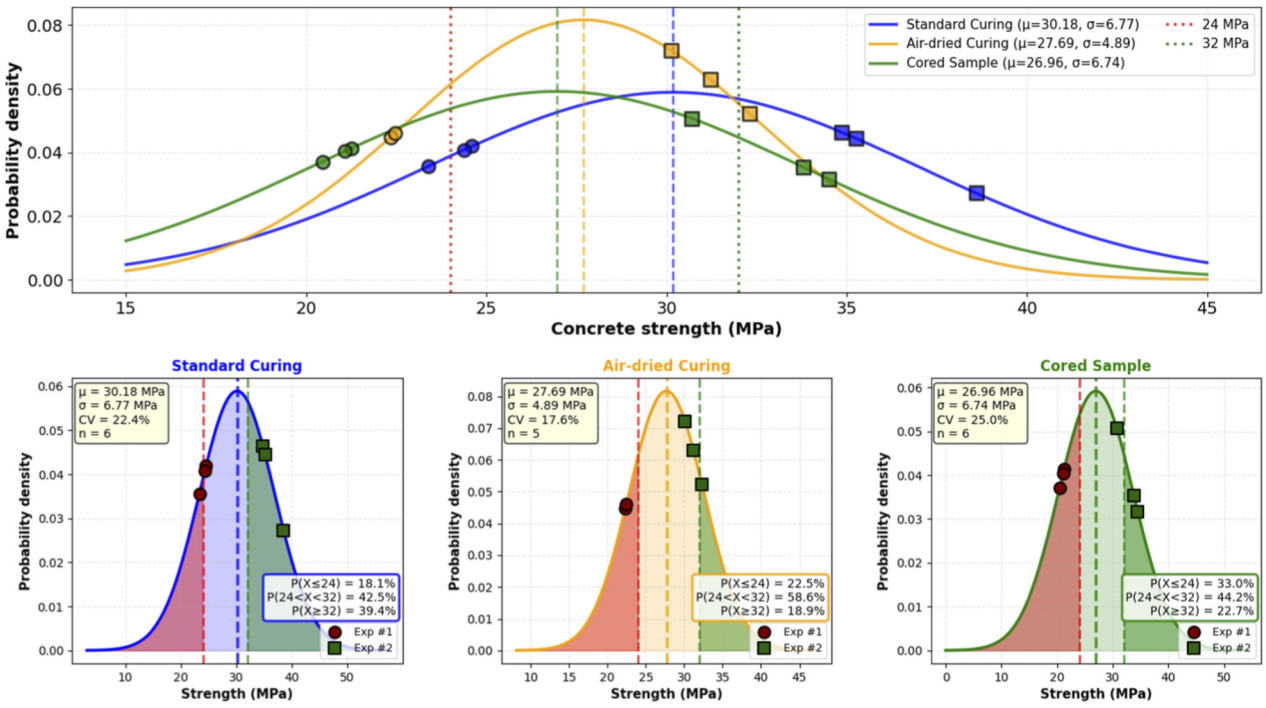

FIGURE 10
Mean strength, standard deviation, covariance for SC, AD, and Cored samples for Exp #1, and #2.

the slab, spaced at intervals of 30 mm to obtain sufficient coverage and reliable data across the surface as shown in Figure 11. The averaged rebound strength 21.9 MPa for Exp #1, 33.4 MPa for Exp #2 showed close to those of cored samples which is 20.9 MPa for Exp #1, 33 MPa for Exp #2 respectively. The rebound hammer test was performed with a 30 mm grid spacing in accordance with ASTM C805/C805M (2018) and KS F 2730 (2018). This spacing was strictly maintained to ensure that each impact point remains unaffected

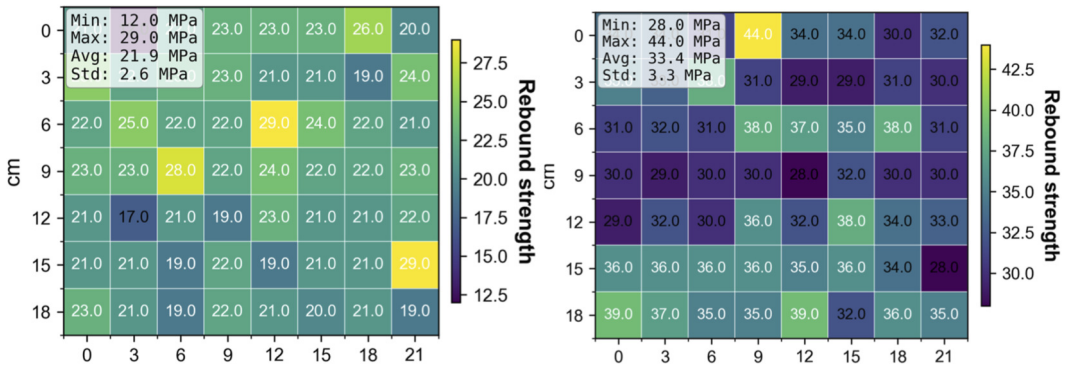

FIGURE 11
Non-destructive strength test results: transformed 56 pointwise rebound strengths evenly spaced in 3.0 in the vicinity of top-center region for Exp #1, and #2.

by previous measurements, thereby securing the reliability of the estimated compressive strength.

3.3 Maturity-strength development

Concrete maturity is a concept that quantifies the combined effects of time and temperature on the strength development of concrete. It provides a way to predict in-place concrete strength without destructive testing. The core idea is that higher temperature reflects the faster hydration and it leads a faster strength gain. The well-known Nurse-Saul linear function is shown in Equation 5.

$$M(t) = \sum (T_a - T_o) \cdot \Delta t \tag{5}$$

Where, M(t): maturity index (°C·hours or °C·days), T_a: average concrete temperature (°C), T_o: datum temperature (usually −10 °C to 0 °C), Δt: time interval (hours). While nonlinear Arrhenius-based maturity index is described as equivalent age in terms of the reference temperature, 20 °C.

$$t_e = \sum \Delta t \,.\, \exp\left(-\frac{E_a}{R}\left(\frac{1}{T_a} - \frac{1}{T_{ref}}\right)\right) \tag{6}$$

Where, t_e = equivalent age at reference temperature (usually 20 °C), E_a = activation energy (38,300 J/mol for Type I cement), R = gas constant (8.314 J/mol·K), T_a, T_{ref}: absolute temperatures (K). In this study, the strength prediction equation specified in ASTM C1074 (2020) is applied to the above cases (Exp #1: hot weather, Exp #2: normal conditions). For Exp #1 (accelerated condition), 17,194 data points were recorded for 670.66 h long. Temperature range was from 24.51 °C–36.32 °C in avg. 27.79 °C. The final maturity (equivalent age), 947.59 h (39.48 days) is equivalent to the chronological age of 28 days. In Exp #2 (retarded condition), 20,148 data points were recorded for 671.57 h long while temperature range was from 13.62 °C–28.75 °C in avg. 16.47 °C. The lower temperatures resulted in a significantly lower equivalent age of 572.11 h (23.8 days) at 28 days as listed in Table 3.

The variables used in the prediction equation, as shown in Equation 7, are expressed in terms of equivalent age. Although an additional maturity evaluation method (Nurse-Saul method) exists, it is excluded from this context due to its simple linear formulation. The equivalent age, M required to achieve the same hydration effect as curing at the reference temperature (typically 20 °C).

$$S = \frac{S_u \times k \times M}{1 + k \times M} \tag{7}$$

Where, S: predicted strength (MPa), S_u: ultimate strength (MPa), k: rate constant (/hrs), M: Arrhenius equivalent age (hrs) defined in Equation 6. To apply Equation 7 defined in ASTM C1074 (2020), S_u and k must be determined from measured data using nonlinear regression through an incremental-iterative solution. This process is carried out via the stepwise iterative procedure outlined below from Equations 8–11.

Step 1: Select trial strength and rate constant, and calculate predicted strength

$$S = \frac{S_u^{trial} \times k^{trial} \times M}{1 + k^{trial} \times M} \tag{8}$$

Step 2: Compute squared strength residuals, SSR against measured values, S_m

$$SSR_i = \sum (S_m - S)^2 \tag{9}$$

Step 3: Perform iterative loop to minimize residuals

$$[\Delta S_u^i, \Delta k^i] = -\nabla^2 SSR_i \cdot \nabla SSR_i \tag{10}$$

Step 4: Update trial strength and rate constant

$$[S_u^{n+1}, k^{n+1}] = [S_u^n + \Delta S_u^i, k^n + \Delta k^i], \Delta S_u^i, \Delta k^i < \text{tol.} = 10^{-6} \tag{11}$$

The strength-maturity relationship was modeled using a hyperbolic function calibrated specifically to the Cored sample data.

TABLE 3 Summary of equivalent age and compressive strength development.

Test No.	Time (Days)	Equivalent age (M = t_e, hours)	SC strength (MPa)	AD strength (MPa)	Cored strength (MPa)
#1	3	123.83	13.89	13.77	13.00
	7	266.22	17.11	16.08	15.90
	28	947.59	24.12	22.41	20.90
#2	1	28.86	-	10.94	-
	3	80.19	23.67	22.07	21.30
	7	163.63	27.91	26.85	27.20
	14	310.15	35.25	28.81	28.73
	28	572.11	36.24	31.21	33.00

SC, standard curing; AD, air-dried curing; Cored, in-situ cored samples.

TABLE 4 Determination for ultimate strength and rate constant for Exp #1, and #2.

Test No.	Ultimate strength (S_u, MPa)	Rate constant (k)	R^2 (Cored)	RMSE (MPa)
#1	22.85	0.0099	0.9788	0.54
#2	32.86	0.0191	0.9606	0.90

This approach prioritizes in-situ structural safety. For Exp #1, The low rate constant (k ≈ 0.01) reflects the slower relative strength gain towards the limiting value in the high-temperature equivalent age scale. Exp #2 Shows a higher limiting strength (S_u≈32.86 MPa) and a significantly different reaction rate constant, influenced by the mixture design and curing environment as listed in Table 4.

Figure 12 shows how these S_u and k determined from the iterative process and its convergence with the tolerance to minimize the residuals. Equation 12 construct the estimated concrete strength from the measured strength data. The measured strengths by age were well-fitted into the Equation 12 for both Exp #1, and Exp #2 respectively.

$$S_{24} = \frac{0.226M}{1 + 0.0099M} \quad S_{32} = \frac{0.628M}{1 + 0.0191M} \tag{12}$$

where, S_u^{24} = 22.85 MPa, k^{24} = 0.0099/hrs, S_u^{32} = 32.86 MPa, k^{32} = 0.0191/hrs

The cored-based model was tested against SC and AD data to evaluate its predictive capability for different curing regimes. The model calibrated on in-situ Cored data provides a reliable lower-bound estimate. It consistently predicts the strength of Air-Dried (AD) samples in Exp #2 with a low average absolute error of 5.25% as listed in Table 5. The Standard Cured (SC) samples consistently exhibited strengths 10%–15% higher than the model prediction in both experiments. This confirms that relying on standard cylinders would overestimate the in-situ structural capacity, validating the necessity of the Cored-based maturity approach for formwork removal. The updated analysis for Exp #2 resulted in a refined rate constant (k = 0.0191) and a higher limiting strength (35.15 MPa), improving the model's fit ($R^2 > 0.96$) and providing a more accurate correlation between the thermal history and strength development.

4 Coupled thermal-stress analysis with humidity-dependent shrinkage

This section implements a semi-empirical equation based on measured data of drying shrinkage strain occurring during the slab curing period. It utilizes the existing drying shrinkage model (Bažant et al., 1972; Bažant et al., 2015; Wendner et al., 2014) and material constants extracted during measurement, combined with modeling of environmental conditions (ambient temperature and relative humidity), mix design conditions based on the target concrete strength of the slab, and the degree of hydration. To analytically validate this, the material constitutive model was simulated using ABAQUS UMAT thermodynamic strain and stress decomposition. The heat of hydration source inducing thermal deformation was implemented using the HETVAL subroutine. Here, state variable linkage ensured effective information transfer between the two subroutines during calculation. Figure 13 shows the flowchart for this process. The UMAT subroutine implements a coupled thermo-mechanical model for early-age concrete behavior based on the Bažant hydration framework. The model captures elastic modulus evolution, autogenous shrinkage, drying shrinkage, and thermal effects during cement hydration.

4.1 Hydration kinetics: UMAT

The fundamental parameter governing concrete maturity is the degree of hydration α(t), which represents the fraction of cement that has reacted with water. The Bažant et al. (2015) model describes this evolution as:

$$\alpha(M) = \alpha_\infty \left[\frac{M}{\tau + M}\right]^\beta \tag{13}$$

where $\alpha(M)$ = degree of hydration at equivalent age, α_∞ = ultimate degree of hydration (typically 0.85–0.90, 0.88 in here), t_{eq} = M = equivalent age (days), τ = hydration time parameter (days), β = hydration shape parameter = 0.85. To account for temperature

10.3389/fmats.2026.1762995

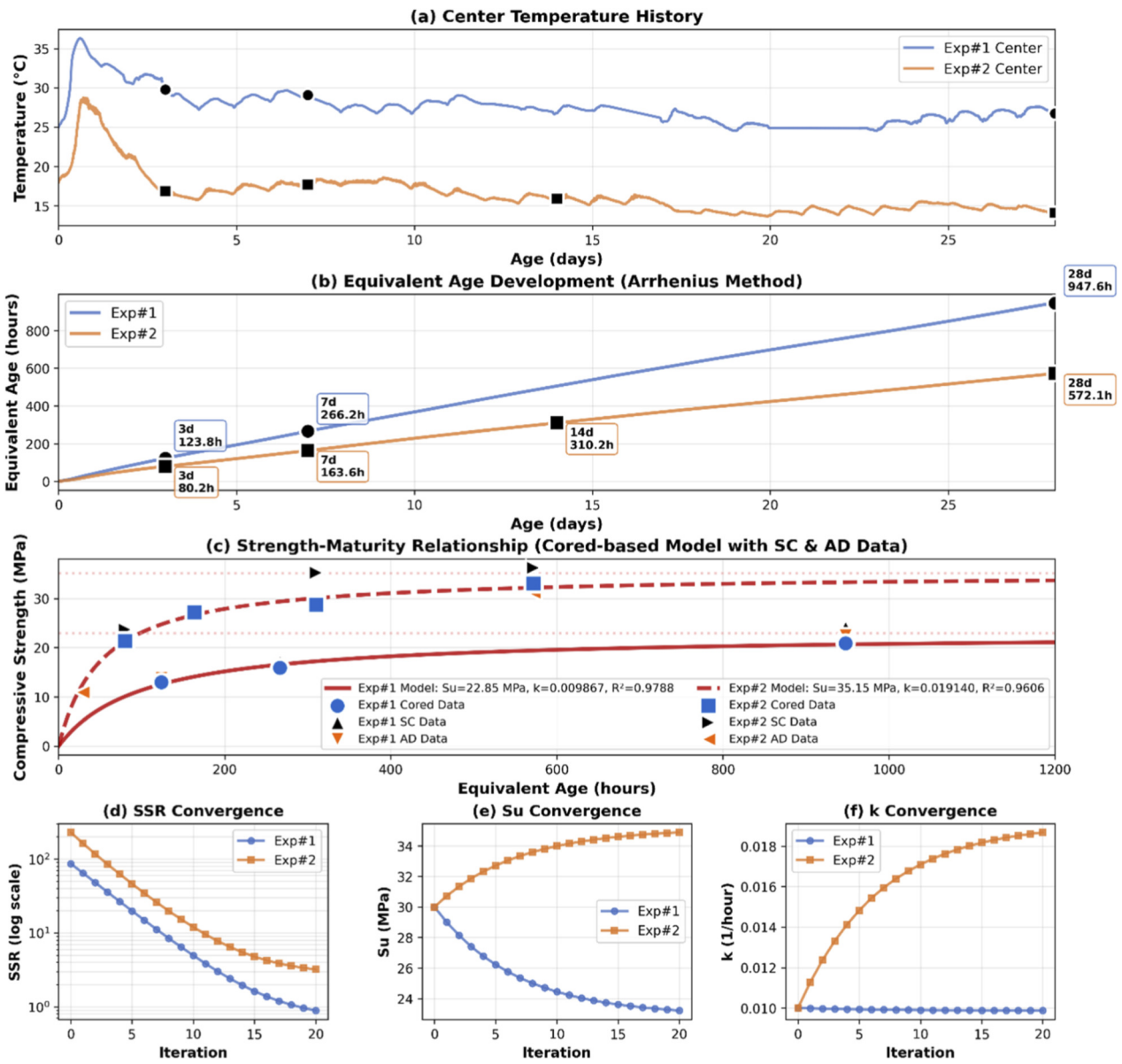

FIGURE 12
Strength prediction using equivalent age, M: **(a)** center temp. History, **(b)** Equivalent age development, **(c)** strength-maturity relationship, **(d)** SSR convergence, **(e)** ultimate strength convergence, and **(f)** rate constant convergence.

effects on hydration rate hydration rate as written in Equation 14, the equivalent age is computed using the Arrhenius equation:

$$dM = dt \cdot \xi(T),\ \xi(T) = e^{\left[\frac{E_a}{R}\left(\frac{1}{T_{ref}}-\frac{1}{T}\right)\right]} \tag{14}$$

where, E_a = activation energy (kJ/mol) = 38,300 J/mol, R = universal gas constant = 8.314 J/(mol·K), Tref = 298.15 K (20 °C), T: Current T (Kelvin), ξ(T): Arrhenius temperature compensation factor ($0.1 \leq \xi \leq 5.0$). The rate of hydration is obtained by time differentiation of Equations 13–15.

$$d\alpha/dM = \alpha_\infty \cdot \beta \cdot \tau/(\tau+M)^2 \cdot [M/(\tau+M)]^{(\beta-1)} \tag{15}$$

The elastic modulus (Powers-Brownyard model) evolves from an initial value E_0 to an asymptotic value E_∞ according to $E(\alpha) = E_0 + (E_\infty - E_0) \times [1 - e^{(-\alpha_E \times \alpha^{\beta_E})}]$, where E(α) = elastic modulus at degree of hydration α, E_0 = initial elastic modulus, E_∞ = final elastic modulus, α_E = calibration parameter, β_E = shape parameter. Where, initial elastic modulus, E_o = 5–10 GPa, ultimate modulus, E_∞ = 30–35 GPa, development rate constant, α_e = 2.5, shape factor for S-curve, β_e = 1.2. Total strain can be written as the summation of elastic strain, hydration heat generated thermal strain, thermo-mechanical shrinkage (autogenous, drying) strain with relative humidity measure as written in Equations 16–19,

$$\varepsilon_{total} = \varepsilon_{elastic} + \varepsilon_{thermal} + \varepsilon_{shrinkage} \tag{16}$$

$$\varepsilon_{shrinkage} = \varepsilon_{au} + \varepsilon_{cd} \tag{17}$$

TABLE 5 Prediction error analysis (Cored vs. SC and AD).

Test No.	Age (Days)	SC prediction error (%)	AD prediction error (%)
#1	3	−9.53%	−8.74%
	7	−3.27%	+2.92%
	28	−14.42%	−7.89%
#2	1	-	+8.23%
	3	−10.08%	−3.56%
	7	−4.54%	−0.77%
	14	−14.66%	+4.42%
	28	−11.12%	+3.20%

$$\varepsilon_{elastic} = \varepsilon_{total} - \alpha_T \cdot \Delta T \cdot \kappa(t) - \left(\varepsilon_{au} + \varepsilon_{cd}\right) \tag{18}$$

$$\sigma = D{:}\varepsilon_{elastic} \tag{19}$$

where, $D_{ijkl} = \lambda \cdot \delta_{ij} \cdot \delta_{kl} + \mu\left(\delta_{ik} \cdot \delta_{jl} + \delta_{il} \cdot \delta_{jk}\right)$, and Lame constants are $\lambda = E \cdot \nu / [(1+\nu)(1-2\nu)], \mu = G = E / [2(1+\nu)]$.

The total shrinkage strain is decomposed into autogenous and drying components with relative humidity measure: (a) autogenous shrinkage strain as written in Equation 20,

$$\varepsilon_{\text{au}} = \varepsilon_{\text{au},\infty} \cdot S(t) \cdot \left[1 - e^{-\sqrt{\left(\frac{t}{\tau_{\text{au}}}\right)}}\right] \text{ for } t \geq 1.0 \text{ days} \tag{20}$$

where, ultimate autogenous shrinkage strain, $\varepsilon_{au,\infty} = -180 \times 10^{-6}$, τ_{au} = 1.2 days, S(t) = saturation factor, t: time after casting (days). (b) drying shrinkage strain (Modified Bažant-Baweja B4 model) as written in Equation 21,

$$\varepsilon_{cd} = \varepsilon_{sh,\infty} \cdot k_h \cdot \text{S(t)} \cdot \text{h(t) for t} \geq 1.5 \text{ days} \tag{21}$$

where, humidity factor, $k_h = 1 - (RH)^3$, ultimate shrinkage strain, $\varepsilon_{sh,\infty} = -250 \times 10^{-6} \cdot [1 + 0.08(\text{W/C} - 0.5)] \cdot \sqrt{35/f_{cm}}$

$$S(t) = \begin{cases} 0.0714t', \ 0 \leq \text{t}' \leq 1.5\text{d} \\ 0.1071 + 0.0251(t' - 1.5), \ 1.5 < \text{t}' \leq 13.5\text{d} \ \leq 1.0 \\ 0.4085 + 0.0112(\text{t}' - 13.5), \ \text{t}' > 13.5\text{d} \end{cases}$$

where $t' = t - 1.5$ days, RH = relative humidity, W/C = water-to-cement ratio, f_{cm} = average 28 days strength, V/S = volume-to-surface ratio. Finally, thermal strain can be written in Equation 22,

$$\varepsilon_{th} = \alpha\text{T} \cdot \Delta\text{T} \cdot \kappa(\text{t}) \tag{22}$$

where ΔT = T - Tref, early compensation factor (limits peak thermal expansion to ~80 με), κ(t) = 0.7 + 0.3(t/3)1.5 for t < 3 days, otherwise κ(t) = 1.0. αT = thermal expansion coefficient, Tref = 20 °C. Drying shrinkage is a critical phenomenon in early-age concrete behavior that significantly affects structural performance and cracking potential. The MC-2010 (2013) provides a comprehensive framework for predicting drying shrinkage, typically assuming shrinkage initiation at 7 days under standard conditions. However, for summer slab conditions with high surface-to-volume ratios and elevated temperatures, drying can commence much earlier, potentially within 12–24 h after casting. The abrupt initiation of shrinkage strain in numerical models often leads to convergence difficulties and computational instability, particularly when using implicit time integration schemes.

4.2 Coupled analysis: heat transfer and drying shrinkage

Previous studies, including those by Ulm and Coussy (1995), Di Luzio and Cusatis (2009), and Cervera et al. (1999), have explored hygro-thermo-chemical modeling to describe the hydration and aging processes of concrete at early ages. Building upon these foundations, this study performs a hygro-thermo-mechanical coupled analysis utilizing the ABAQUS UMAT subroutine. The HETVAL (Heat Value) subroutine calculates volumetric heat generation rate due to cement hydration. This implements a realistic temperature evolution profile targeting experimental observations. Three-Phase Heat Release was adopted: Phase 1: Rapid Rise to Peak (0 ≤ t ≤ 0.3 days), Phase 2: Exponential Decay (0.3 < t ≤ 2.0 days), Phase 3: Long-term Saturation (t > 2.0 days) as illustrated in Figure 14. The gradual drying shrinkage model is implemented through a user-defined material subroutine (UMAT) that handles the mechanical behavior of early-age concrete. The subroutine integrates targeting the following temperature profile: initial 25 °C (ambient casting temperature), peak 36 °C at 0.3 days (7.2 h), intermediate 32 °C at 3 days, saturated in 30 °C for Exp #1. The heat generation from HETVAL drives the temperature field through the heat conduction as written in Equation 23,

$$\rho c \times \partial T/\partial t = \nabla \cdot (k \nabla T) + Q(t, T) \tag{23}$$

where, ρ = density (kg/m^3), c = specific heat (J/(kg·K)), k = thermal conductivity (W/(m·K)), Q(t,T) = volumetric heat generation from HETVAL, The temperature field T(x,t) is then passed to UMAT to calculate: Equivalent age and degree of hydration, elastic modulus evolution, thermal strains, resulting stresses. Figure 15 shows the heat of hydration rise, cooled-down, and saturated to the ambient temperature. von-Mises stress, total strain, nodal temperature distribution were shown.

5 Machine learning model for strength prediction

In recent years, ML–based maturity prediction has developed as a next-generation framework for assessing concrete strength and informing construction decisions. Unlike traditional models that are either oversimplified (Nurse–Saul) or computationally restrictive (Arrhenius), ML models can integrate diverse datasets, capture nonlinear dependencies, and adapt to variable curing scenarios. For practical adoption, the framework proposed in this study is designed to satisfy three essential requirements: (i) physical interpretability, ensuring compliance with international standards such as ACI 318–19, EN 206:2013, JSCE, and KCS 14 20 12; (ii) data adaptability, enabling robust predictions across different binder systems, mix

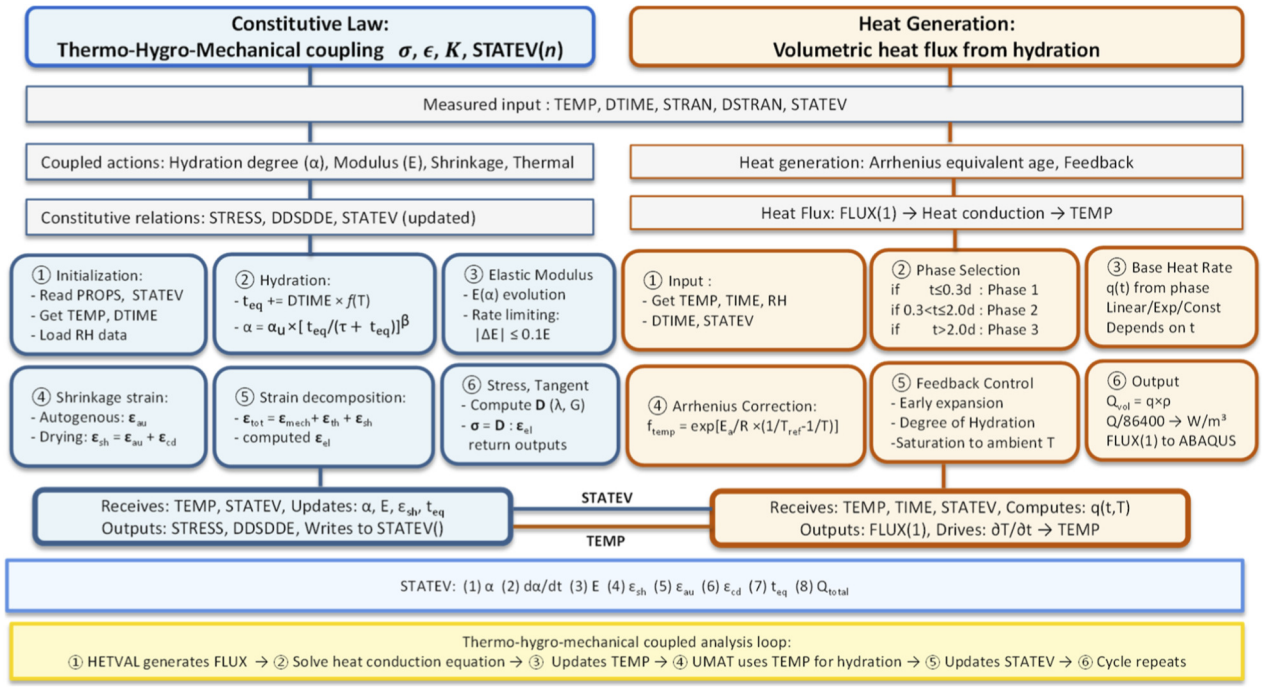

FIGURE 13
Flowchart for UMAT and HETVAL subroutines for thermo-mechanical analysis.

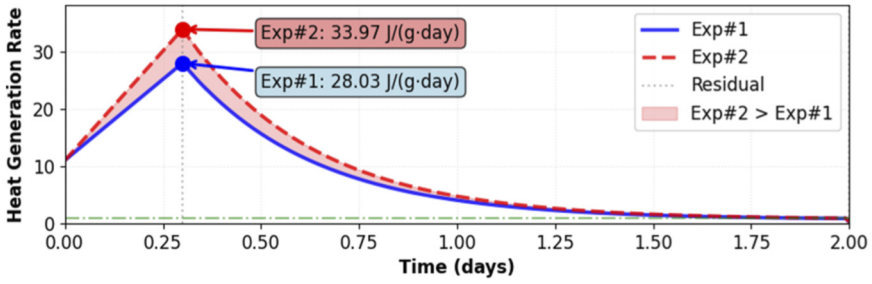

FIGURE 14
Heat generation rate for Exp #1, and #2.

proportions, and environmental conditions; and (iii) AI scalability, supporting integration of both experimental and in-situ monitoring data for broader generalization. Maturity-based approaches are already embedded in international practice. In the United States, the maturity method is standardized in ASTM C1074 (2020) and applied with ACI 318 and ACI 347R, where formwork striking is generally permitted once the concrete reaches approximately 70% of specified design compressive strength of concrete ($f'c$), corresponding to maturity values of 300 °C–400 °C·h for normal-strength concrete. In Europe, EN 13670 (Execution of Concrete Structures) and EN 1992-1-1 (Eurocode 2) allow early striking based on verified in-situ strength, commonly 2–5 MPa or 50%–70% of $f'c$, with maturity values of 200 °C–500 °C·h. Japanese code, guided by JSCE-GC No. 16, typically requires a minimum of 5 MPa strength and maturity ≥300 °C·h before removal. In Korea, the Korean Concrete Institute (2012) and KCS 14 20 12 specify stricter criteria, mandating that striking occurs only when concrete reaches ≥ max(14 MPa, 2/3 $f'c$) and that shores are removed only at 100% $f'c$, although in slab practice a practical limit of 5 MPa with ~300 °C·h maturity is often applied.

To achieve these technical objectives, the study first formulates a baseline maturity-strength model by calibrating ML algorithms using a reference concrete mix (target compressive strength 24 MPa, without admixtures) to serve as a controlled benchmark for predictive performance. This predictive domain is subsequently expanded through the incorporation of heterogeneous datasets covering multiple mix proportions, binder systems, and strength classes, enabling the framework to account for complex nonlinear relationships across diverse material compositions. To ensure engineering reliability, physical consistency constraints are integrated by embedding code-based thresholds and acceptance criteria derived from international standards,

10.3389/fmats.2026.1762995

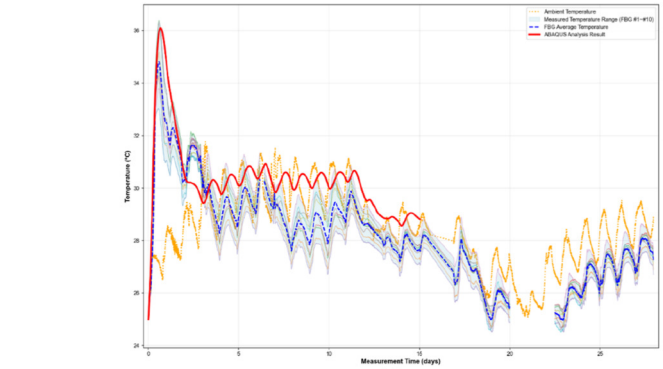

(a)

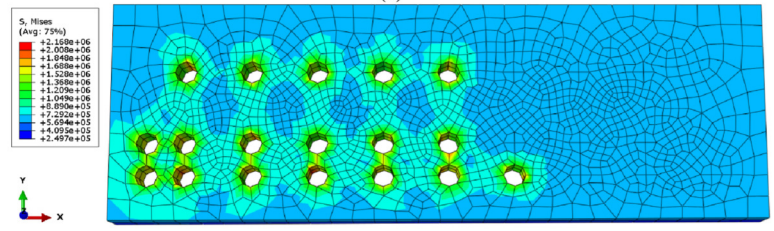

(b)

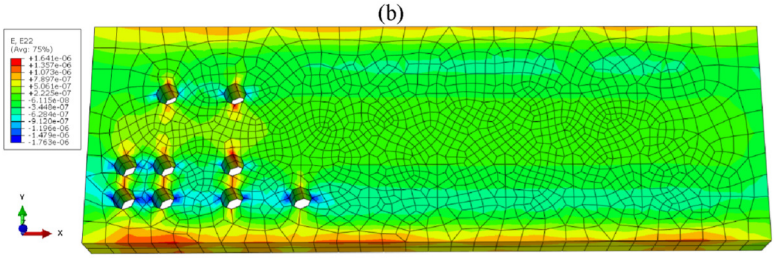

(c)

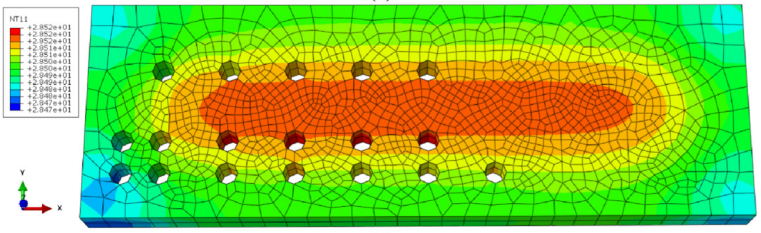

(d)

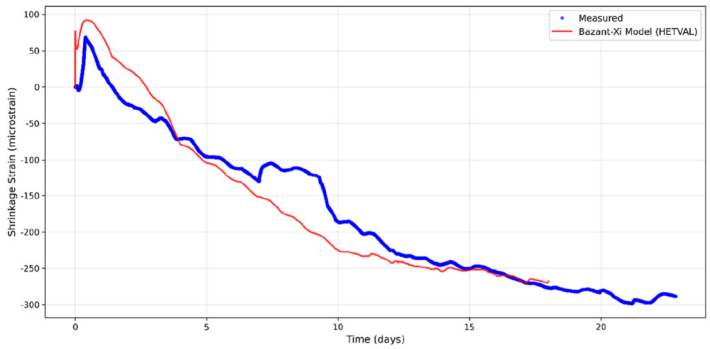

(e)

FIGURE 15
Heating-and-Cooling process due to heat of hydration for Exp #1, and #2: **(a)** Coupled analysis temperature history results, **(b)** von-Mises stresses, **(c)** total strains, **(d)** temperature distribution, **(e)** total strain measured vs. Bažant et al. model with HETVAL under relative humidity history for Exp #1.

ensuring that predictions remain aligned with established design provisions. Concurrently, the study quantifies data adaptability by systematically evaluating model accuracy under variable curing environments—including differing temperature profiles, humidity, and boundary conditions—thereby assessing its robustness under realistic field conditions. The framework's model transferability is then demonstrated through the integration of experimental datasets with in-situ monitoring streams from IoT-enabled maturity sensors, validating its ability to extend predictions from laboratory-controlled to construction-scale scenarios. Ultimately, these efforts culminate in the derivation of decision-support criteria for formwork strike and shore removal timing, expressed in terms of maturity-equivalent ages and predicted strength thresholds, to directly link ML-based outputs with construction scheduling and safety requirements.

5.1 ML model for maturity-based strength prediction

A comparison of ML algorithms was conducted to identify the optimal approach for predicting concrete compressive strength from degree-day (DD) maturity data. The dataset comprised 55 experimental measurements (Ryu et al., 2024) including maturity indices, temperature histories, and mix design parameters (W/B, w/c, cement content) as listed in Table 6. Feasibility analysis was performed to capture nonlinear strength development characteristics, generating derived variables including square root of DD, log-scaled time, and equivalent Nurse-Saul maturity. Features with absolute correlation coefficients exceeding 0.3 with the target strength were selected for model training. Six ML algorithms were systematically evaluated: Ridge regression ($\alpha = 1.0$ and $\alpha = 0.1$), Lasso regression ($\alpha = 0.5$), ElasticNet, Random Forest, and Gradient Boosting. Model performance was assessed using leave-one-out cross-validation (LOO-CV) to ensure robust evaluation given the limited dataset size. Three primary metrics were computed: root mean squared error (RMSE) from LOO-CV, coefficient of determination (R^2), and mean absolute error (MAE). Figure 16 presents the comparative performance across all models. Gradient Boosting achieved the lowest RMSE of 1.88 MPa with near-perfect R^2 (1.000), while Random Forest exhibited similar predictive capability (RMSE = 2.95 MPa, $R^2 = 0.957$). Linear regularization methods showed moderate performance, with Ridge ($\alpha = 0.1$) achieving RMSE of 2.03 MPa. An ensemble model combining the top three performers (Gradient Boosting, Ridge $\alpha = 0.1$, and Random Forest) was constructed, yielding RMSE of 1.82 MPa and R^2 of 0.973. The predicted versus actual strength relationships demonstrate excellent agreement for all models, with the ensemble approach providing the most balanced performance.

Residual analysis (Figure 17) reveals that all models exhibit minimal systematic bias (mean residuals near zero), with standard deviations ranging from 1.26 MPa (Ensemble) to 2.88 MPa (ElasticNet). The dataset comprised 55 measurements compiled from the literature. However, the Gradient Boosting model achieved a perfect R^2 of 1. In this limited dataset ($n = 55$), such a result must be interpreted as clear evidence of overfitting rather than superior performance. This phenomenon occurs because the model, trained on a small-scale and localized dataset, 'memorizes' specific noise and data patterns instead of learning generalized physical relationships. Furthermore, the literature-based dataset primarily relies on ambient curing temperatures and total durations. The systematic underprediction observed at early ages (1–3 days) highlights a fundamental gap: external environmental data cannot accurately reflect the internal hydration heat history that governs early-age kinetics. This discrepancy confirms that monitoring in-situ core temperature history is a prerequisite for reliable maturity-based assessment. To mitigate overfitting, future work must focus on acquiring larger datasets that synchronize internal core temperatures with precise curing ages. Feature importance analysis using Random Forest (Figure 18) reveals that maturity-related parameters dominate the prediction capability. The DD maturity index and its square root transformation account for approximately 85% of the total feature importance (0.45 and 0.40, respectively), while mix design variables (w/c and cement content) contribute only 12% combined. This finding confirms that temperature-time history is the primary driver of strength development, with mix proportions playing a secondary role in the prediction model.

Both Gradient Boosting and the ensemble approach closely follow the experimental measurements from early age (4 MPa at ~100 h) through long-term development (25 MPa at ~36,000 h), demonstrating consistent predictive accuracy across the full maturity range. In Figure 19, The ensemble method exhibits the most balanced profile, achieving high scores in R^2 (0.97), inverted RMSE (0.90), and inverted MAE (0.89), indicating superior overall performance without significant weaknesses in any single metric. Based on this comprehensive evaluation, the ensemble approach is recommended as the optimal model for this dataset. While Gradient Boosting shows the lowest LOO-CV RMSE, its perfect R^2 value (1.000) suggests potential overfitting to the training data. The ensemble method provides a more conservative and generalizable solution by combining multiple algorithms, effectively mitigating individual model weaknesses. The RMSE of 1.82 MPa represents approximately 5%–8% prediction error relative to typical 28-day strengths (25–35 MPa), which is acceptable for practical engineering applications. However, the limited dataset size ($n = 55$) necessitates caution in extrapolating beyond the observed maturity and strength ranges, and validation with independent test data is recommended before field implementation. Figure 20 provides an overall assessment of the Gradient Boosting (GB) model for predicting concrete compressive strength from maturity data. The figure contains four panels analyzing different aspects of model performance. The predicted vs. measured plot shows that the model generally follows the 1:1 line, with most points within the ±10% tolerance. Performance metrics indicate good overall accuracy (RMSE = 3.84 MPa, MAE = 3.26 MPa, $R^2 = 0.7466$, MAPE = 14.9%), although the model slightly underpredicts higher-strength specimens. The error-by-age panel shows that early-age predictions exhibit the largest negative errors (−5.37 MPa at 1 day and −2.64 MPa at 3 days). Errors decrease substantially at 7 and 14 days, suggesting that the model captures the general strength development trend but struggles during the rapid early-age hydration phase. The strength development curves illustrate that the model reproduces the overall nonlinear growth pattern. However, early-age measured strengths exceed predictions, while convergence occurs at later ages (e.g., 31.0 MPa measured vs. 30.9 MPa predicted at 28 days).

10.3389/fmats.2026.1762995

TABLE 6 55 tailored dataset for concrete maturity from the literature (Ryu et al., 2024).

Time	T_o	T_a	RH	S/a	W/C	W	C	S	G	T_c	SP	f'_c	Slump	AC	DD
237.12	23	5	95	50	0.5	165	330	891	901	5	0.19	5.9	180	4.5	49.4
538.08	23	5	95	50	0.5	165	330	891	901	5	0.19	10.1	180	4.5	112.1
754.56	23	5	95	50	0.5	165	330	891	901	5	0.19	12	180	4.5	157.2
1,047.36	23	5	95	50	0.5	165	330	891	901	5	0.19	13.8	180	4.5	218.2
3,695.52	23	5	95	50	0.5	165	330	891	901	5	0.19	23.3	180	4.5	769.9
240.48	23	5	95	49.5	0.45	169	370	856	884	5	0.48	7.4	180	4.5	50.1
541.44	23	5	95	49.5	0.45	169	370	856	884	5	0.48	14.1	180	4.5	112.8
753.12	23	5	95	49.5	0.45	169	370	856	884	5	0.48	17.5	180	4.5	156.9
1,049.28	23	5	95	49.5	0.45	169	370	856	884	5	0.48	20.1	180	4.5	218.6
3,677.28	23	5	95	49.5	0.45	169	370	856	884	5	0.48	28.9	180	4.5	766.1
246.72	23	5	95	49	0.41	172	410	840	867	5	0.62	8.1	180	4.5	51.4
534.72	23	5	95	49	0.41	172	410	840	867	5	0.62	16.3	180	4.5	111.4
755.52	23	5	95	49	0.41	172	410	840	867	5	0.62	19.3	180	4.5	157.4
1,047.84	23	5	95	49	0.41	172	410	840	867	5	0.62	23	180	4.5	218.3
3,768	23	5	95	49	0.41	172	410	840	867	5	0.62	36	180	4.5	785
237.12	23	5	95	49	0.55	172	349	821	864	5	0.6	3.8	180	4.5	49.4
514.56	23	5	95	49	0.55	172	349	821	864	5	0.6	9.4	180	4.5	107.2
728.16	23	5	95	49	0.55	172	349	821	864	5	0.6	11.8	180	4.5	151.7
1,010.4	23	5	95	49	0.55	172	349	821	864	5	0.6	16	180	4.5	210.5
3,556.32	23	5	95	49	0.55	172	349	821	864	5	0.6	24.6	180	4.5	740.9
236.64	23	5	95	49	0.55	172	287	810	853	5	0.6	3.6	180	4.5	49.3
513.6	23	5	95	49	0.55	172	287	810	853	5	0.6	8	180	4.5	107
726.72	23	5	95	49	0.55	172	287	810	853	5	0.6	10.6	180	4.5	151.4
1,008.48	23	5	95	49	0.55	172	287	810	853	5	0.6	13.5	180	4.5	210.1
3,549.12	23	5	95	49	0.55	172	287	810	853	5	0.6	23	180	4.5	739.4
40.32	23	20	95	50	0.5	165	330	891	901	20	0.19	7.8	180	4.5	33.6
77.76	23	20	95	50	0.5	165	330	891	901	20	0.19	10.9	180	4.5	64.8
113.64	23	20	95	50	0.5	165	330	891	901	20	0.19	12.9	180	4.5	94.7
260.88	23	20	95	50	0.5	165	330	891	901	20	0.19	17.3	180	4.5	217.4
1,048.68	23	20	95	50	0.5	165	330	891	901	20	0.19	24.5	180	4.5	873.9
40.68	23	20	95	49.5	0.45	169	370	856	884	20	0.48	9.1	180	4.5	33.9
78.48	23	20	95	49.5	0.45	169	370	856	884	20	0.48	14.5	180	4.5	65.4
114.72	23	20	95	49.5	0.45	169	370	856	884	20	0.48	17.1	180	4.5	95.6
262.92	23	20	95	49.5	0.45	169	370	856	884	20	0.48	22.6	180	4.5	219.1
1,051.92	23	20	95	49.5	0.45	169	370	856	884	20	0.48	30.2	180	4.5	876.6
40.92	23	20	95	49	0.41	172	410	840	867	20	0.62	12.4	180	4.5	34.1
78	23	20	95	49	0.41	172	410	840	867	20	0.62	16.9	180	4.5	65
115.08	23	20	95	49	0.41	172	410	840	867	20	0.62	20.5	180	4.5	95.9
271.56	23	20	95	49	0.41	172	410	840	867	20	0.62	26.9	180	4.5	226.3
1,059.36	23	20	95	49	0.41	172	410	840	867	20	0.62	35.6	180	4.5	882.8
30.54	23	40	95	50	0.5	165	330	891	901	40	0.19	10.4	180	4.5	50.9

(*Continued*)

10.3389/fmats.2026.1762995

TABLE 6 Continued

Time	T_o	T_a	RH	S/a	W/C	W	C	S	G	T_c	SP	f'_c	Slump	AC	DD
60.78	23	40	95	50	0.5	165	330	891	901	40	0.19	12.8	180	4.5	101.3
91.08	23	40	95	50	0.5	165	330	891	901	40	0.19	15.4	180	4.5	151.8
121.32	23	40	95	50	0.5	165	330	891	901	40	0.19	17	180	4.5	202.2
424.68	23	40	95	50	0.5	165	330	891	901	40	0.19	20.7	180	4.5	707.8
30.48	23	40	95	49.5	0.45	169	370	856	884	40	0.48	12.5	180	4.5	50.8
56.58	23	40	95	49.5	0.45	169	370	856	884	40	0.48	16	180	4.5	94.3
83.64	23	40	95	49.5	0.45	169	370	856	884	40	0.48	18.4	180	4.5	139.4
111.12	23	40	95	49.5	0.45	169	370	856	884	40	0.48	20.6	180	4.5	185.2
413.04	23	40	95	49.5	0.45	169	370	856	884	40	0.48	25.5	180	4.5	688.4
32.16	23	40	95	49	0.41	172	410	840	867	40	0.62	15.7	180	4.5	53.6
62.7	23	40	95	49	0.41	172	410	840	867	40	0.62	20.2	180	4.5	104.5
93.12	23	40	95	49	0.41	172	410	840	867	40	0.62	22.3	180	4.5	155.2
123.42	23	40	95	49	0.41	172	410	840	867	40	0.62	24	180	4.5	205.7
427.98	23	40	95	49	0.41	172	410	840	867	40	0.62	34.8	180	4.5	713.3

Time (hours), T_o:initial temp (°C), T_a: ambient temp (°C), RH: relative humidity (%), W/B: water-to-binder, S/a: Sand ratio, W/C: water-to-cement ratio, W: water (kg), C: cement (kg), S: sand (kg), G: gravel (kg), T_c: curing temp (°C), SP: superplasticizer, f'_c: concrete strength (MPa), Slump (mm), AC: air content (%), DD: degree-day (°C·day).

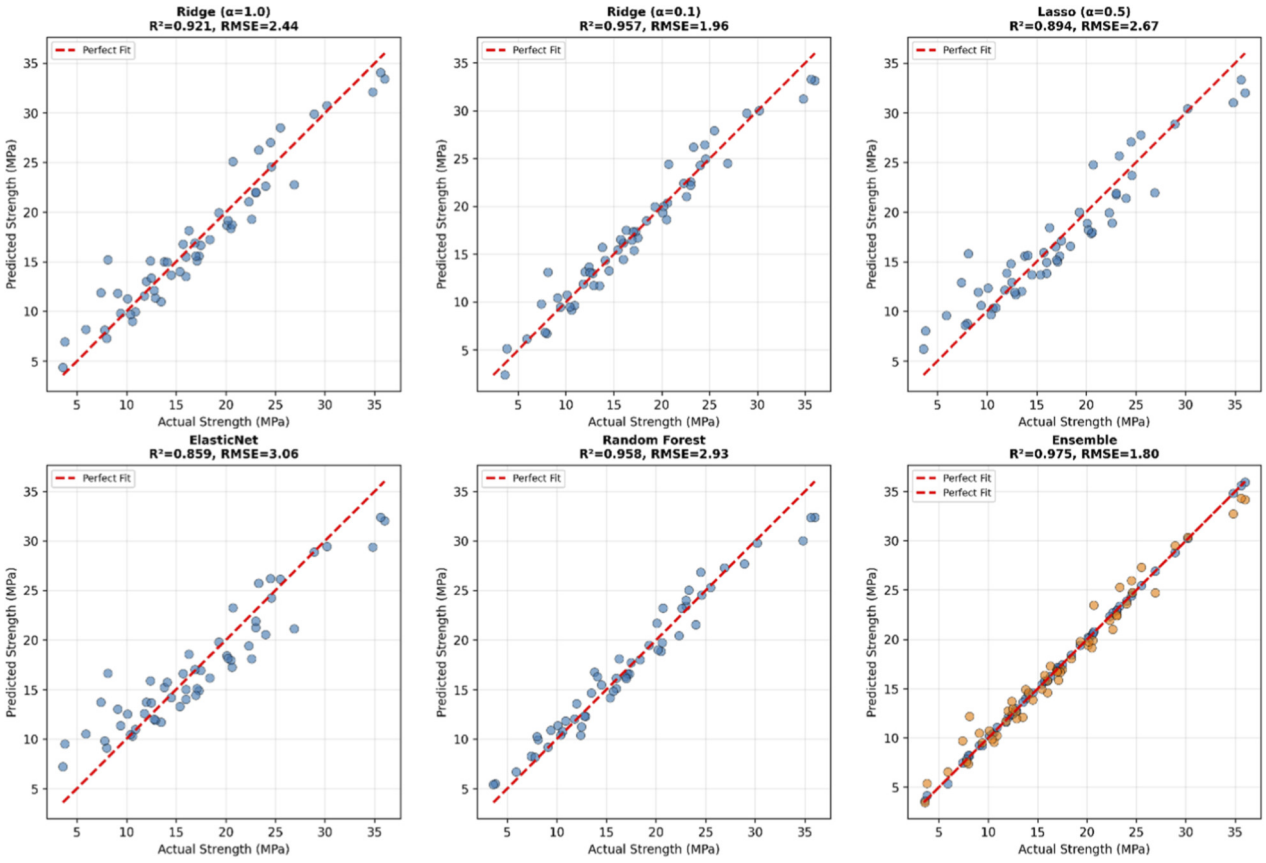

FIGURE 16
Six ML algorithms for prediction vs. actual strength: Ridge regression (α = 1.0 and α = 0.1), Lasso regression (α = 0.5), ElasticNet, Random Forest, and Gradient Boosting.

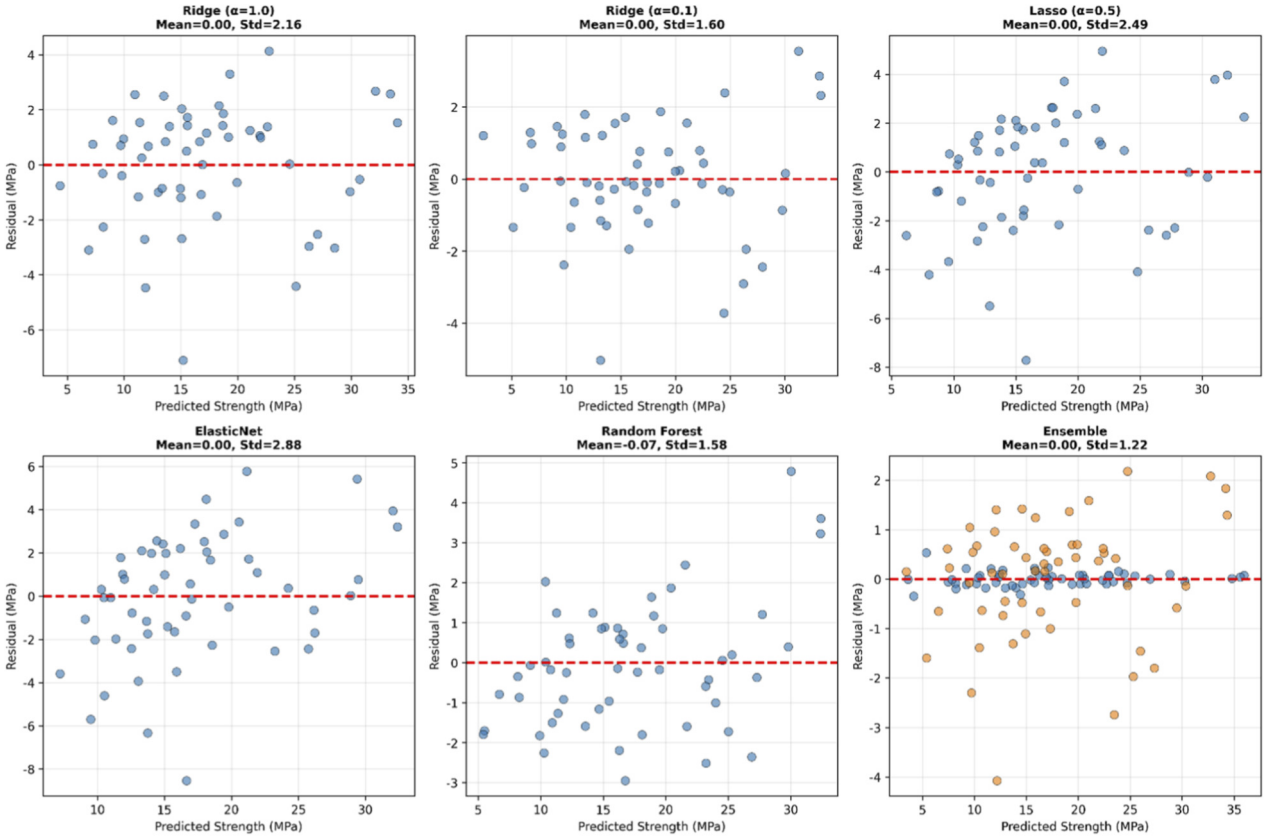

FIGURE 17
Six ML algorithms: residuals against predicted strength.

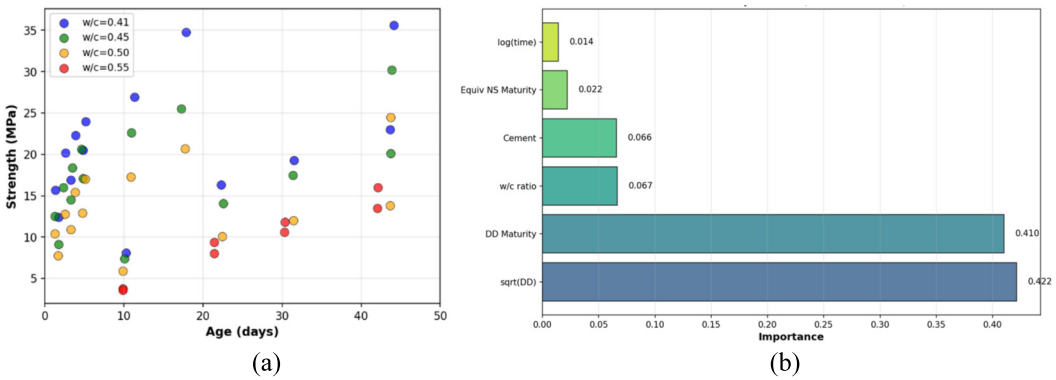

FIGURE 18
Random Forest feature analysis: **(a)** tailored 55 dataset, **(b)** feature importance.

The percentage error panel confirms large early-age deviations (27.8% at 1 day, 19.7% at 3 days), with accuracy improving significantly at later ages (9.2% at 14 days, 2.1% at 28 days). Although the overall MAPE is 14.9%, this masks substantial age-dependent variations. Overall, the GB model performs reasonably well, especially after 7 days. However, notable systematic underprediction occurs at early ages, when hydration kinetics are highly nonlinear. Improved early-age prediction would require additional early-age training data or hydration-specific features to achieve the ±10% accuracy commonly required for engineering applications.

5.2 Discuss and future studies

This study compared ML algorithms to identify the optimal approach for predicting concrete compressive strength from degree-day (DD) maturity data. The current dataset comprises 55 experimental measurements compiled from the literature. It is

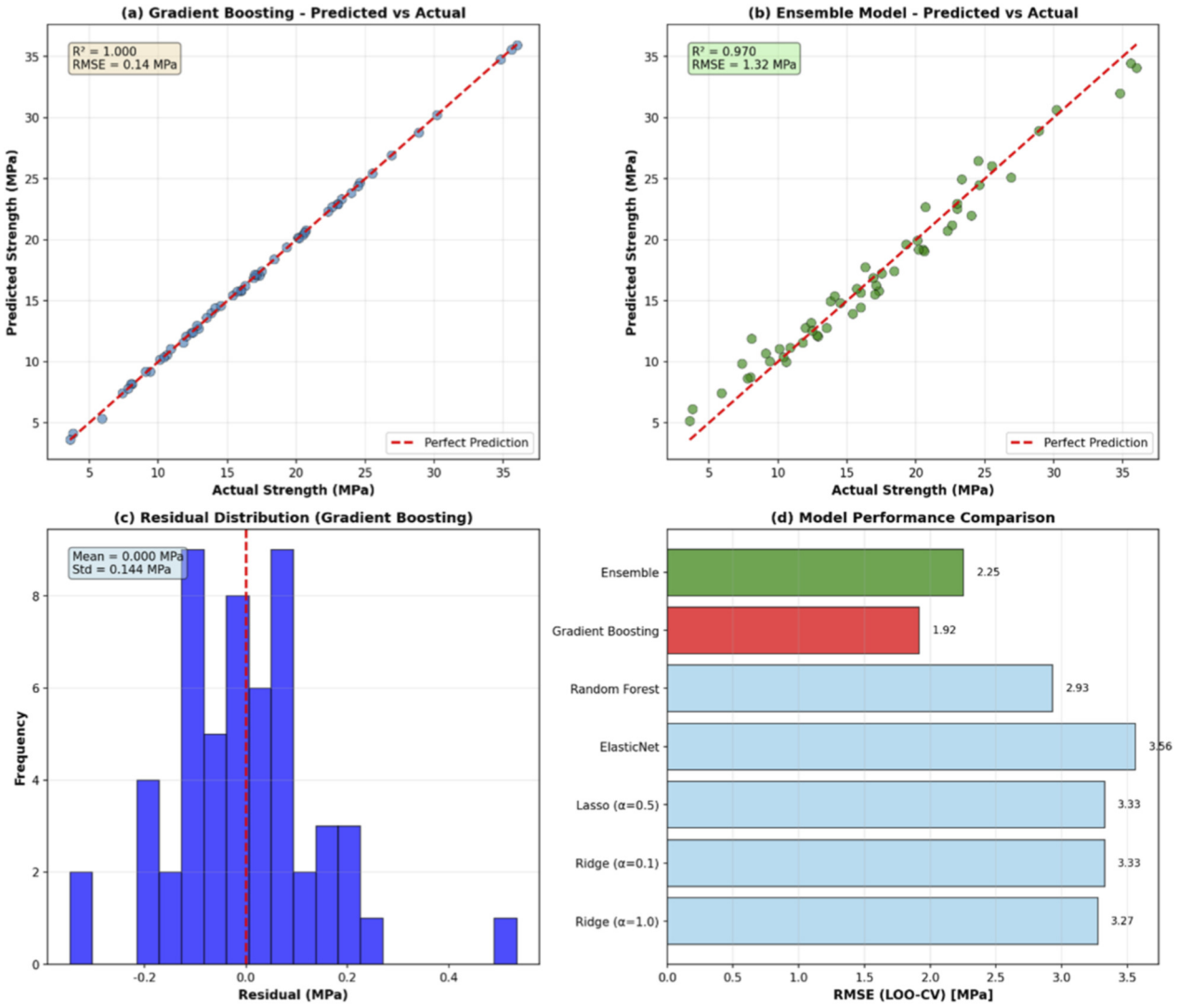

FIGURE 19
Ensemble and Gradient Boosting approach: predicted vs. actual **(a)** GB, **(b)** Ensemble, **(c)** Residual distribution, GB, and **(d)** Model performance in terms of RMSE.

crucial to note that this dataset primarily relies on ambient curing temperatures and total durations rather than direct in-situ core temperature monitoring.

Analysis of Model Overfitting The Gradient Boosting (GB) model achieved a perfect R^2 value of 1. In the context of a small-scale dataset ($n = 55$), this result should be interpreted as clear evidence of overfitting rather than superior predictive performance. Given the data scarcity, the non-linear model likely *memorized* specific noise or localized data points within the limited training range, thereby compromising its generalizability to unseen data.

Importance of Core Temperature Measurement The systematic errors observed in early-age strength predictions—specifically the significant deviations at 1 to 3 days—highlight the fundamental limitations of the current dataset. Because the existing data is based on external ambient conditions, it fails to capture the internal hydration heat history that drives early-age strength gain. This discrepancy reinforces the critical necessity of monitoring in-situ core temperature history for accurate maturity-based assessments.

Future Research and Data Acquisition To mitigate overfitting and enhance the reliability of the ML framework, acquiring a larger and more specialized dataset that includes synchronized internal core temperature records and precise curing ages is essential. This study serves as an exploratory proof-of-concept; future research will focus on securing extensive experimental data through advanced sensing to improve the model's robustness and field applicability.

6 Conclusion

This study proposes a comprehensive decision-making framework for the optimal formwork removal of concrete slabs, integrating FBG sensing technology, thermo-mechanical coupled analysis, and ML algorithms. The key findings and contributions are

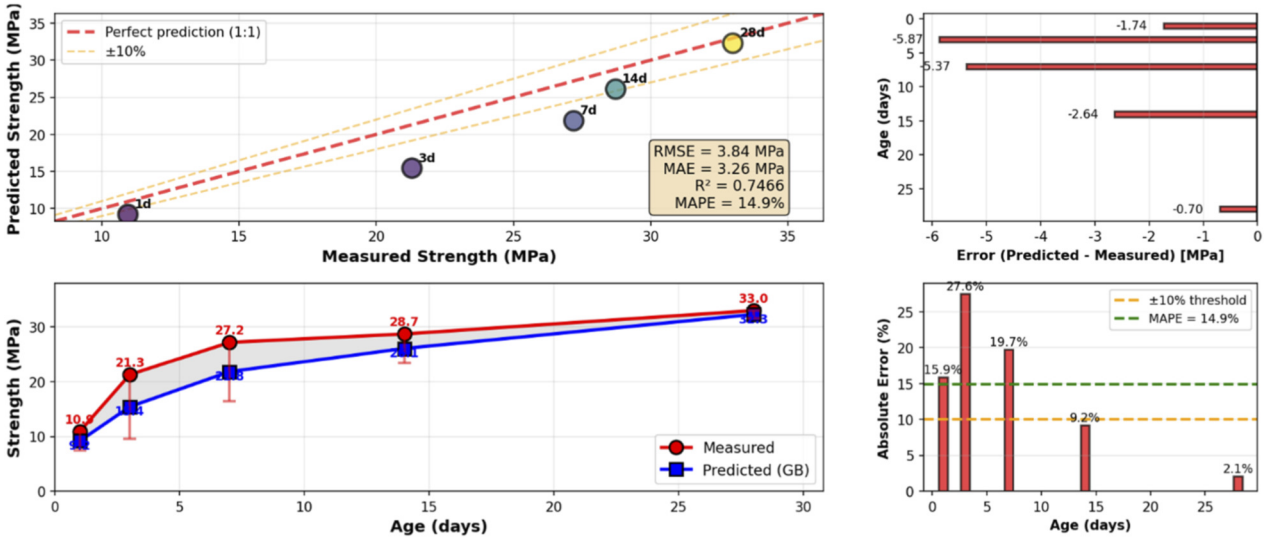

FIGURE 20
ML Prediction using Gradient Boosting approach for Exp #2.

summarized as follows: First, the efficacy of the developed stainless-steel (SUS) packaged FBG sensors was validated. The packaging successfully decoupled thermal expansion from mechanical strain, ensuring precise monitoring of hydration heat and drying shrinkage even under harsh curing conditions. Second, a thermo-hygro-mechanical coupled analysis using user subroutines (UMAT and HETVAL) in ABAQUS accurately simulated the early-age behavior of concrete. The model effectively captured the evolution of temperature fields, degree of hydration, and resulting stress distributions, aligning well with experimental observations. Third, while the ML-based prediction showed potential, the high risk of overfitting (R^2 = 1.0) due to the small dataset (n = 55) was identified as a major technical challenge. The significant errors in early-age strength gain were attributed to the reliance on ambient environmental data rather than internal hydration records. This underscores the critical importance of the in-situ core temperature monitoring system developed in this study. In conclusion, the proposed framework serves as a rational proof-of-concept, and future research will focus on securing larger datasets through IoT-based in-situ monitoring to enhance the model's scalability and robustness.

Data availability statement

The raw data supporting the conclusions of this article will be made available by the authors, without undue reservation.

Author contributions

H-JP: Conceptualization, Funding acquisition, Project administration, Writing – original draft, Writing – review and editing. YC: Data curation, Investigation, Writing – original draft, Writing – review and editing. D-GK: Conceptualization, Formal Analysis, Investigation, Project administration, Writing – original draft, Writing – review and editing. IR: Data curation, Formal Analysis, Investigation, Software, Validation, Visualization, Writing – original draft, Writing – review and editing.

Funding

The author(s) declared that financial support was received for this work and/or its publication. This work was supported by internal fund of Electronics and Telecommunications Research Institute (ETRI). (26ZK1100, Honam region regional industry-based ICT convergence technology advancement support project).

Conflict of interest

The author(s) declared that this work was conducted in the absence of any commercial or financial relationships that could be construed as a potential conflict of interest.

Generative AI statement

The author(s) declared that generative AI was not used in the creation of this manuscript.

Any alternative text (alt text) provided alongside figures in this article has been generated by Frontiers with the support of artificial intelligence and reasonable efforts have been made to ensure accuracy, including review by the authors wherever possible. If you identify any issues, please contact us.

Publisher's note

References

ACI 318-19 (2025). *Building code requirements for structural concrete*. Farmington Hills, MI: American Concrete Institute.

ACI PRC-347-14 (2021). *Guide to formwork for concrete*. Farmington Hills, MI: American Concrete Institute.

ACI 228.1R-19 (2019). *Report on methods for estimating concrete strength*. Farmington Hills, MI: American Concrete Institute.

ASTM C805/C805M (2018). *Standard test method for rebound number of hardened concrete*. West Conshohocken, PA: ASTM International.

ASTM C1074 (2020). *Standard practice for estimating concrete strength by the maturity method*. West Conshohocken, PA: ASTM International.

Bakhoum, E. S., Amir, A., Osama, F., and Adel, M. (2023). Prediction model for the compressive strength of green concrete using cement kiln dust and FA. *Sci. Rep.* 13, 1864. doi:10.1038/s41598-023-28965-4

Bažant, Z. P., and Najjar, L. J. (1972). Nonlinear water diffusion in nonsaturated concrete. *Mater. Struct.* 5 (1), 3–20. doi:10.1007/bf02479073

Carino, N. J., and Lew, H. S. (2001). "The maturity method: from theory to application," in *Structures 2001: a structural engineering Odyssey* Reston, VA: American Society of Civil Engineers). doi:10.1061/40558(2001)17

Carino, N. J., and Tank, R. C. (1990). "Maturity functions for concrete made with various cements and admixtures," in *Testing during concrete construction: proceedings of RILEM colloquium*. Editor H. Rusch (Boca Raton, FL: CRC Press), 192–200.

Cervera, M., Oliver, J., and Prato, T. (1999). Thermo-chemo-mechanical model for concrete. I: hydration and aging. *J. Eng. Mech.* 125 (9), 1018–1027. doi:10.1061/(asce)0733-9399(1999)125:9(1018)

Chen, Y. (2007). *Accelerated ageing tests and long-term prediction models for durability of FRP bars in concrete*. Morgantown, WV, USA: West Virginia University. Ph.D. Thesis.

Cheng, Y. H., Zhu, B. L., Yang, S. H., and Tong, B. Q. (2021). Design of concrete mix proportion based on particle packing voidage and test research on compressive strength and elastic modulus of concrete. *Materials* 14, 623. doi:10.3390/ma14030623

Chengju, G. (1989). Maturity of concrete: method for predicting early-stage strength. *ACI Mat. J.* 86, 341–353. doi:10.14359/2099

De Schutter, G., and Taerwe, L. (1996). Degree of hydration-based description of mechanical properties of early age concrete. *Mater. Struct.* 29, 335–344. doi:10.1007/bf02486341

Dewan, R., Polishetty, R., Sharan, B., Goyal, M. K., Balde, A. M., and Greynoon, A. M. A. (2023). "Cement strength prediction using regression techniques," in *Proceedings of the 2023 10th international conference on computing for sustainable global development (INDIACom)* (Piscataway, NJ: IEEE), 75–80.

Di Luzio, G., and Cusatis, G. (2009). Hygro-thermo-chemical modeling of high-performance concrete. I: theory. *Cem. Conc. Com.* 31 (5), 301–308. doi:10.1016/j.cemconcomp.2009.02.015

Di Palma, P., De Vita, E., Iadicicco, A., and Campopiano, S. (2022). Force sensor based on FBG embedded in silicone rubber. *IEEE Sensors J.* 23 (23–2), 1172–1178. doi:10.1109/JSEN.2022.3226039

EN 13670 (2009). *Execution of concrete structures*. European Committee for Standardization.

EN 206 (2013). *Concrete–Specification, performance, production and conformity*. European Committee for Standardization.

Han, F., and Zhang, Z. (2016). Hydration, mechanical properties and durability of high-strength concrete under different curing conditions. *J. Therm. Anal. Calorim.* 132, 823–834. doi:10.1007/s10973-017-6377-1

He, J., Xu, B., Xu, X., Liao, C., and Wang, Y. (2021). Review of femtosecond-laser-inscribed fiber bragg gratings: fabrication technologies and sensing applications. *Photonic Sensors* 11, 203–226. doi:10.1007/s13320-021-0629-2

Hill, K. O., and Meltz, G. (2002). Fiber bragg grating technology fundamentals and overview. *J. Lightw. Technol.* 15–8, 1263–1276. doi:10.1109/50.618320

Imran, H., Al-Abdaly, N. M., Shamsa, M., Shatnawi, A., Ibrahim, M., and Ostrowski, K. (2022). Development of prediction model to predict the compressive strength of eco-friendly concrete using multivariate polynomial regression combined with stepwise method. *Materials* 15, 317. doi:10.3390/ma15010317

Ji, S., Li, K., Yuan, P., Sun, G., Lu, L., Meng, F., et al. (2022). Design and fabrication of AWG with large bandwidth applied in FBG interrogation system. *Opt. Laser Technol.* 149, 107372. doi:10.1016/j.optlastec.2021.107372

Jin, N. J., Yeon, K. S., Min, S. H., and Yeon, J. (2017). Using the maturity method in predicting the compressive strength of vinyl ester polymer concrete at an early age. *Adv. Mat. Sci. Eng.* 2017, 4546732. doi:10.1155/2017/4546732

JSCE-GC No. 16(2007). *JSCE Standard specifications for concrete structures-2007: materials and construction*(Tokyo, Japan: JSCE).

Kampli, G., Chickerur, S., and Chitawadagi, M. V. (2023). Real-time *in-situ* strength monitoring of concrete using maturity method of strength prediction *via* IoT. *Mat. Today Proc.* 88, 110–118. doi:10.1016/j.matpr.2023.02.480

Kazemifard, S., Motaghed, S., and Eftekhari, N. (2024). NDT prediction of self-compacting concrete strength based on maturity method. Multiscale multidiscip. *Model. Exp. Des.* 7, 1031–1043. doi:10.1007/s41939-024-00277-5

Kim, S., Jung, D., Kim, J.-Y, and Mun, J.-H (2024). Study on early age concrete's compressive strengths in unmanaged curing condition using IoT-based maturity monitoring. *Buildings* 14 (3), 798. doi:10.3390/buildings14030798

Kim, H., Park, S., Yeo, C., Kang, H. S., and Park, H.-J. (2021). Thermal analysis of 22.9-kV crosslinked polyethylene cable joint based on partial discharge using fiber Bragg grating sensors. *Opt. Eng.* 60 (3),034101. doi:10.1117/1.OE.60.3.034101

Korean Concrete Institute (KCI) (2012). *Korean Construction specification (KCS 14 20 12): concrete structures standard specification. Ministry of land*. Korea: Infrastructure, and Transport.

KS F 2730 (2018). *Testing method for rebound number of concrete*. Korea: Korean Agency for Technology and Standards.

Li, C., Tang, J., Cheng, C., Cai, L., and Yang, M. (2021). FBG arrays for quasi-distributed sensing: a review. *Phot. Sensors* 11–1, 91–108. doi:10.1007/s13320-021-0615-8

McIntosh, J. D. (1956)."Effect of low-temperature curing on the compressive strength of concrete," in Proceedings of the RILEM Symposium: Winter Concreting, Copenhagen, Session BII, 17.

Miller, D., Ho, N. M., Talebian, N., and Javanbakht, Z. (2023). Real-time monitoring of early-age compressive strength of concrete using an IoT-enabled monitoring system: an investigative study. *Innov. Infrastruct. Solut.* 8, 75. doi:10.1007/s41062-023-00976-w

Qiao, H., Lin, Z., Sun, X., Li, W., Zhao, Y., and Guo, C. (2023). Fiber optic-based durability monitoring in smart concrete: a state-of-art review. *Sensors* 23–18, 7810. doi:10.3390/s23187810

Rusna, K. P., and Kalpana, V. G. (2022). Using artificial neural networks for the prediction of the compressive strength of geopolymer FA. *Eng. Technol. Appl. Sci. Res.* 12, 9120–9125. doi:10.48084/etasr.5120

Ryu, G.-S., An, G.-H., Yoon, Y.-S., Kim, J.-Y., and Choi, S. (2024). Evaluation of concrete compressive strength prediction using the maturity method incorporating various curing temperatures and binder compositions. *Materials* 17 (23), 5794. doi:10.3390/ma17235794

Tank, R. C., and Carino, N. J. (1991). Rate constant functions for strength development of concrete. *ACI Mat. J.* 88 (1), 74–83. doi:10.14359/2403

Ulm, F. J., and Coussy, O. (1995). Modeling of thermochemomechanical couplings of concrete at early ages. *J. Eng. Mech.* 121 (7), 785–794. doi:10.1061/(asce)0733-9399(1995)121:7(785)

Wang, L., Wu, L., and Fang, C. (2019). Study on applicability of maturity theory to predict concrete compressive strength under non-standard curing condition. *IOP Conf. Ser. Earth Environ. Sci.* 304, 052115. doi:10.1088/1755-1315/304/5/052115

Wendner, R., Hubler, M. H., and Bažant, Z. P. (2014). "Model B4: multi-decade creep and shrinkage prediction of traditional and modern concretes," in *Computational modelling of concrete structures* (London, United Kingdom: Taylor & Francis Group), 679–684.

Yang, K. H., Mun, J. S., Kim, D. G., and Cho, M. S. (2016). Comparison of strength–maturity models accounting for hydration heat in massive walls. *Int. J. Concr. Struct. Mat.* 10, 47–60. doi:10.1007/s40069-016-0132-0